NASA TECHNICAL NOTE

NASA TN D-3917

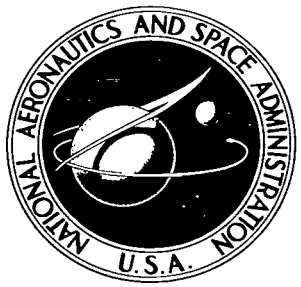

STABILITY AND DRAG CHARACTERISTICS AT MACH NUMBERS OF 10 AND 26 OF A PROPOSED SLENDER ATMOSPHERIC PROBE

by Gerald N. Malcolm

Ames Research Center
Moffett Field, Calif.

NATIONAL AERONAUTICS AND SPACE ADMINISTRATION • WASHINGTON, D. C. • APRIL 1967

NASA TN D-3917

STABILITY AND DRAG CHARACTERISTICS AT MACH NUMBERS OF 10 AND 26 OF A PROPOSED SLENDER ATMOSPHERIC PROBE

By Gerald N. Malcolm

Ames Research Center
Moffett Field, Calif.

NATIONAL AERONAUTICS AND SPACE ADMINISTRATION

For sale by the Clearinghouse for Federal Scientific and Technical Information
Springfield, Virginia 22151 – CFSTI price $3.00

STABILITY AND DRAG CHARACTERISTICS AT MACH NUMBERS OF 10 AND 26 OF A PROPOSED SLENDER ATMOSPHERIC PROBE

By Gerald N. Malcolm

Ames Research Center

SUMMARY

Free-flight tests at Mach numbers 10 and 26 were conducted on models of a slender, flare-stabilized cone cylinder proposed by Goddard Space Flight Center for use as a Mars-atmosphere probe. The tests were conducted to determine drag, stability, and flow-field characteristics in both nose-forward and nose-rearward attitudes. Results of nose-forward tests at Mach numbers of 10 and 26 and at Reynolds numbers of 0.6×10^6 showed extremely nonlinear but stable pitching-moment characteristics. The stability at low angles of attack (due, at least in part, to the observed laminar-boundary-layer separation over the cylinder and flare) decreased rapidly with increasing angle of attack until the bow-shock wave approached the windward side of the flare. Further increasing the angle of attack produced a notable increase in stability. No significant Mach number effects were observed in either the stability or drag results. Tests results at a Mach number of 10 showed the configuration was unstable in the nose-rearward attitude. The pitching moment for the model in this attitude was deduced from the rotational acceleration of the model. The pitching moment for the entire angle-of-attack range from $\alpha = 0^\circ$ to $\alpha = 180^\circ$ was determined by extrapolation of the experimental results from nose-forward and nose-rearward tests plus an iterative improvement of the extrapolation by a technique which matches a synthesized motion to several cycles of an observed free-flight motion. Models of the probe were found to be dynamically stable at all angles of attack tested.

INTRODUCTION

The design of an instrumented soft lander for exploration of the Martian surface is strongly dependent upon the characteristics of the Martian atmosphere through which it must fly and which decelerates the lander helping to bring it to rest at the surface. Atmospheric probe missions to precede the lander mission in which the entry vehicle would, in effect, take soundings of the Martian atmosphere and relay the measurements to Earth prior to impact are therefore being considered.

One approach, proposed by Goddard Space Flight Center, would use a slender flare-stabilized entry vehicle on which measurements of impact and static pressures, accelerations, and mass spectra of gas samples would be interpreted in terms of atmosphere characteristics. In support of the Goddard effort, the hypersonic aerodynamics of models of the slender-body probe have

been investigated at the Ames Research Center in the prototype hypervelocity free-flight facility and the pressurized ballistic range. Two points were of particular interest. The first was to verify that the probe configuration was statically unstable in the nose-rearward attitude and had only one stable nose-forward trim attitude. This is important since the body would be entering the atmosphere passively and therefore could be at any angle of attack. The test conditions corresponded to a combination of the highest Mach number and lowest Reynolds number feasible for testing, and they simulated approximately the high-altitude portion of a Martian entry. The second major point of interest was the aerodynamic characteristics of the probe shape in the nose-forward attitude at high Mach number and Reynolds number simulating the low-altitude portion of the entry where the atmospheric measurements would be made. Drag and static and dynamic stability were determined from measurements of model attitude and position on shadowgraphs. The shadowgraphs were also used for flow visualization. The pitching-moment coefficients for the entire angle-of-attack range from 0° to 180° were determined by extrapolating experimental data for the nose-forward and nose-rearward attitudes and then improving the extrapolations by an iterative technique based on matching a synthesized oscillatory motion to an observed free-flight motion.

SYMBOLS

A	frontal area based on d, cm^2
C_D	drag coefficient, $\frac{\text{drag}}{q_\infty A}$, dimensionless
C_{D_o}	drag coefficient at zero angle of attack, dimensionless
C_{l_α}	lift-curve slope, per radian
C_m	pitching-moment coefficient, $\frac{\text{pitching moment}}{q_\infty Ad}$, dimensionless
$C_{m_{\alpha_l}}$	quasilinear value of pitching-moment-curve slope, $\frac{8\pi^2 I}{\lambda^2 \rho Ad}$, per radian
$(C_{m_q} + C_{m_{\dot{\alpha}}})$	damping-in-pitch derivative, $\frac{\partial C_m}{\partial(qd/V)} + \frac{\partial C_m}{\partial(\dot{\alpha}d/V)}$, per radian
CMQ	modified dynamic-stability parameter, $\xi - C_D$, dimensionless
d	maximum diameter of model (flare), cm
I	moment of inertia about a transverse axis through the center of gravity, $m\sigma^2 \times 10^{-7}$, $kg\text{-}m^2$
$k_{1,2,3}$	constants in equation (1), deg

m	mass of model, gm
M	Mach number, dimensionless
q	pitching velocity, radians/sec
q_∞	free-stream dynamic pressure, newtons/m^2
R	Reynolds number based on maximum diameter and free-stream conditions, dimensionless
t	flight time, sec
V	velocity along flight path, m/sec
V_i	initial velocity (at $t = 0$), m/sec
x	distance along flight path, m
X_{cg}	axial distance from model base to center-of-gravity position, cm
α	angle of attack (in the vertical plane), deg
α_m	average value of maximum-angle envelope, $\frac{\alpha_{max_i} + \alpha_{max_f}}{2}$, deg (see sketch (a))
α_{min}	average value of minimum-angle envelope, $\frac{\alpha_{min_i} + \alpha_{min_f}}{2}$, deg (see sketch (a))
α_{rms}	root-mean-square angle of oscillation, $\sqrt{\frac{1}{x}\int_0^x \alpha_R^2 \, dx}$, deg
α_R	$\sqrt{\alpha^2 + \beta^2}$, deg
β	angle of sideslip (in the horizontal plane), deg
$\eta_{1,2}$	damping exponents in equation (1), m^{-1}
λ	wavelength of pitching oscillation, m/cycle
ρ	free-stream air density, kg/m^3
σ	radius of gyration about a transverse axis through the center of gravity, cm
ξ	dynamic-stability parameter, $C_D - C_{L_\alpha} + (C_{m_q} + C_{m_{\dot{\alpha}}})\left(\frac{d}{\sigma}\right)^2$, dimensionless
φ'	roll parameter, $\frac{\text{roll rate}}{\text{velocity}}$, radians/m

$\omega_{1,2}$ rates of rotation of vectors which describe the model pitching motion in equation (1), radians/m

$( )'$ first derivative with respect to x

$( )''$ second derivative with respect to x

$(\dot{})$ first derivative with respect to time

MODELS, TEST CONDITIONS, AND DATA REDUCTION

Figure 1 is a detailed sketch of the model tested. The diameter d was 0.508 cm for the models and 25.9 cm for the full-scale vehicle. To position the center of gravity of the models to match that of the full-scale vehicle, the models were constructed from two materials joined approximately at the center of gravity. The first models had aluminum afterbodies and sintered tungsten-iron-nickel composition forebodies. The two materials were held together by a steel machine screw. Initial flight tests revealed an undesirable spallation of tungsten particles from the tip of the conical nose because of high heating rates; later models were constructed with tantalum-tungsten alloy forebodies to eliminate this problem. As seen in figure 1, the bases of the models had two cylindrical cavities which were also scaled from the full-sized vehicle. Figure 2 is a photograph of the models and the two types of sabots used - one for nose-forward tests and the other for nose-rearward tests.

All models were gun-launched from deformable piston light-gas gun. Time-distance histories and attitude histories were recorded at spark shadowgraph stations along the flight path. Except for one flight in the pressurized ballistic range (which has 24 stations along a 62-meter length) at $M \sim 10$ and $R \sim 0.02 \times 10^6$, all flights in the nose-forward attitude were made in the prototype hypervelocity free-flight facility (which has 11 stations along a 12.1-meter length) at Mach numbers of 10 and 26 and Reynolds numbers from 0.55×10^6 to 0.67×10^6. (One partial flight was made at $M = 10$ with $R = 0.15 \times 10^6$.) The $M = 10$ tests were made in still air, and the $M = 26$ tests in a countercurrent airstream.

Three nose-rearward flights were made in the pressurized ballistic range at Mach numbers from 7.0 to 9.2 and at Reynolds numbers from 0.009×10^6 to 0.165×10^6. The physical characteristics of the models and the respective flight conditions for each test are summarized in table I. Tests were not conducted in gas compositions containing CO_2, a more appropriate gas for a Martian atmosphere, because (1) the present investigation was not intended to be a comprehensive study of gas composition effects; (2) air as a medium is much simpler to use, especially at $M = 26$ where a countercurrent flow is necessary.

Stability Data-Reduction Methods

Nose-forward tests.- Stability data in the nose-forward attitude were obtained from conventional analyses of the attitude histories of the models. Examples of the pitch-yaw motions experienced by the models are shown in figure 3. Figure 3(a) shows a nearly planar motion and figure 3(b) shows a precessing elliptical type of motion. The numbered symbols show the angles of attack and sideslip measured from the shadowgraphs at each of the stations. (Motions shown represent flight segments of seven stations each.) The curves are fitted to the data points by a method which will be discussed below. A physical interpretation of this type of plot is to imagine oneself looking along the flight path of an approaching model and observing the path that would be traced by the nose of the model as it oscillated about its center of gravity and precessed about its flight path. The majority of the flights exhibited nearly planar motion with little precession.

To obtain the static-stability parameter or quasilinear value of pitching-moment-curve slope, $C_{m_{\alpha_l}}$, and the dynamic-stability parameter (ref. 1)

$$\xi = C_D - C_{L_\alpha} + (C_{m_q} + C_{m_{\dot{\alpha}}})(d/\sigma)^2$$

from the attitude histories, the motion equation developed in reference 2 (further discussed in refs. 3 and 4) was used. Specifically, the tricyclic equation

$$\beta + i\alpha = k_1 e^{(\eta_1 + i\omega_1)x} + k_2 e^{(\eta_2 - i\omega_2)x} + k_3 e^{i\varphi' x} \qquad (1)$$

was fitted by the method of least squares to the measured values of α and β for each flight. The exponents $\omega_{1,2}$ are related to the wavelength of oscillation by

$$\lambda = \frac{2\pi}{\sqrt{\omega_1 \omega_2}}$$

and the exponents $\eta_{1,2}$ are related to ξ by

$$\xi = \frac{\eta_1 + \eta_2}{\rho A/2m}$$

The curves in figure 3 represent best fits of equation (1) to the data.

To identify the amplitude of oscillation of each flight for analysis and presentation of the data, both the minimum and the maximum angles of oscillation must be considered because the angle range through which the models oscillated differed for each flight. The amplitudes are defined in sketch (a).

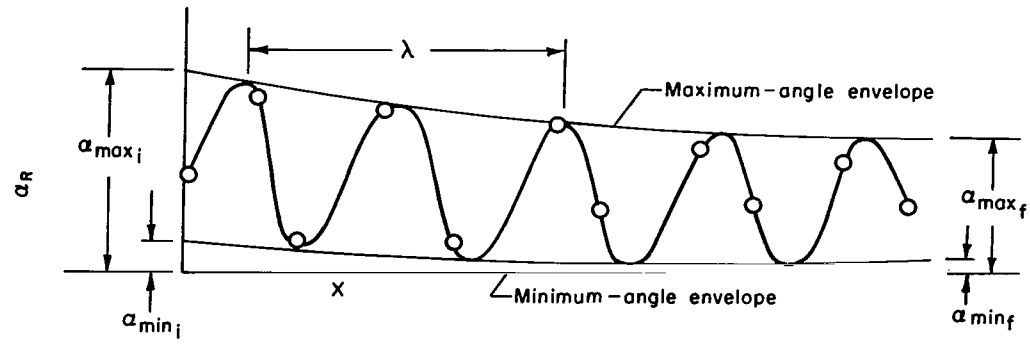

$$\alpha_m = \frac{\alpha_{max_i} + \alpha_{max_f}}{2}, \quad \alpha_{min} = \frac{\alpha_{min_i} + \alpha_{min_f}}{2}, \quad \alpha_{rms} = \sqrt{\frac{1}{x}\int_0^x \alpha_R^2 \, dx}$$

Sketch (a)

The method of data reduction using equation (1) is based on linear aerodynamics (thus a constant wavelength, λ); therefore, for bodies with highly nonlinear stability characteristics, these quasilinear measurements are further reduced by a method developed in reference 5, which takes into account the observed nonlinearities, and a curve of pitching moment versus angle of attack is obtained. A complete explanation of how the results of reference 5 are applied to the present investigation is presented in the appendix.

Where there was a sufficient amount of oscillatory motion in one flight and a marked difference in wavelength or drag was observed over the distance of the flight, the flight record was split into two separate overlapping flight segments for data reduction. Not all of the flights could be split in this fashion, but almost all of the M = 10 flights were. The exceptions are noted later. The typical motions seen in figure 3 are portions of two flights rather than the entire flights themselves.

Nose-rearward tests.- Since the model was presumed initially to be statically unstable in the nose-rearward attitude, it was decided that the pitching moment would have to be deduced directly from the pitch acceleration of the model as it rotated away from the unstable attitude and toward the stable position of $\alpha = 0^\circ$. Because of restrictions on gun placement with respect to the shadowgraph stations and unavoidable sabot interference upon launch, the initial pitching motion of the model from the $\alpha = 180^\circ$ position in the gun could not be measured, so the test was designed to obtain as many shadowgraphs as possible the second time the model was in the vicinity of $\alpha = 180^\circ$ (one-half cycle of motion from the initial launch position). A well-defined angle of attack versus flight-distance curve was obtained with a least squares fit of a polynomial in x to the data in the vicinity of $\alpha = 180^\circ$ (either at the first observable amplitude peak of an oscillatory motion about $\alpha = 0^\circ$ or at $\alpha = 180^\circ$ if the model passed through $\alpha = 180^\circ$ in a slow tumbling motion produced by unsymmetric sabot separation). The equation of

motion governing the behavior of the model, if aerodynamic damping is neglected and velocity loss is small is

$$I\alpha'' = \frac{\rho A d}{2} C_m$$

where

$$\alpha'' = \frac{d^2\alpha}{dx^2}$$

Near peak amplitude, α' is small, and the aerodynamic damping and drag effects (which are proportional to α') can quite properly be neglected. If the variation, $\alpha = f(x)$ (where x is flight distance) can be determined to represent the motion, it can be differentiated twice to obtain

$$\alpha'' = f''(x) = \frac{\rho A d}{2I} C_m$$

or

$$C_m = \frac{2I}{\rho A d} f''(x)$$

We therefore have equations for α and C_m as polynomials in x. These equations then can be used to produce a curve of C_m versus α for the range of α being considered.

RESULTS AND DISCUSSION

Flow Fields

Pertinent features of the flow fields around the models will be described first for later reference in a discussion of the stability data.

Shadowgraphs of a model in the nose-forward attitude at $M = 10$ and $R = 0.6 \times 10^6$ at angles of attack from 0° to 2° are presented in figure 4(a). The shadowgraphs clearly show flow separation over the cylindrical part of the body and part of the flare. At $\alpha = 0^\circ$ the point of separation appears to be slightly behind the cone-cylinder junction. As the angle of attack increases to 2°, the flow over the cylinder and flare gradually becomes essentially attached on the windward side and fully separated on the leeward side. Another important characteristic is that the flow over the entire body is laminar, as can be verified by examination of the wake detail in the original pictures.

The observed bulge in the bow-shock wave is caused by slight blunting of the conical tip. (The model tip was blunted slightly initially to conform to full-scale geometry, and became slightly blunter in flight because of erosion

of the heated nose. Erosion is greater in the tests at M = 26. These shadowgraphs are all from the same flight of a model with a tantalum-tungsten nose. There is very little change in tip geometry over the length of the flight. For comparison, figure 4(b) shows shadowgraphs of a model at M = 10, $R = 0.6 \times 10^6$ with a sintered tungsten-iron-nickel composition nose. The first shadowgraph was taken early in the flight and shows laminar separated flow over the cylinder, as does figure 4(a). The second shadowgraph was taken at the last station in the flight and shows that the nose material has begun to melt, creating what appears to be turbulent flow, or possibly laminar flow containing liquid iron and solid tungsten particles. The nose has been significantly blunted. The tests involving these models will be pointed out later in discussing the data and will be referred to as those with "turbulent" flow.

Figure 5 shows a series of four shadowgraphs of a model at M = 26 and $R = 0.6 \times 10^6$ ranging in angle of attack from 8° to 14°. The major point illustrated is the movement of the bow-shock wave toward the windward side of the flare as the angle of attack is increased. At α near 12°, the bow shock appears to impinge on the flare. The streak in the shadowgraph for $\alpha = 14.2^\circ$ is a streak in the test section window and not a vortex streak as might be suggested.

Figure 6 shows a group of shadowgraphs of a model at M = 26, $R = 0.6 \times 10^6$, and low angles of attack. Although the report reproductions may not be sufficiently clear, the original negatives show evidence of separated flow, similar to that observed at M = 10. This similarity in observed flow fields suggests that over this Mach number range, at low angles of attack, the flow characteristics are insensitive to Mach number. This provides some justification for analyzing the M = 10 and 26 data together.

Drag

Drag coefficients were computed for each flight by least-squares fitting the following equation to the time, t, and flight distance, x, measurements recorded at each data station

$$t = \frac{1}{V_i k C_D} \left(e^{kC_D x} - 1 \right) \qquad \text{(ref. 6)}$$

where $k = (\rho A/2m)$. The drag coefficient, C_D, and initial velocity, V_i, are the coefficients determined from the fit. Figure 7 shows the drag coefficient plotted against α_{rms}, the root-mean-square angle of attack, for all flights. Each of the flights at M = 10, except the two with models that had spalling nose material and the one conducted at low Reynolds number, was split into two flight segments for data-reduction purposes because of the large variation of C_D with α_{rms}. The M = 26 flights did not experience enough cycles of motion to be split. The data point at low Reynolds number was obtained from a flight at low air density with very limited time-distance information; the degree of uncertainty in this point is illustrated by the scatter bar. A curve has been faired through the data points in figure 7. For comparison, a least-squares

fit of a quadratic equation to all the data except the three filled points is shown also. A quadratic fit, commonly used to represent drag data for linear systems, is seen to be a rather poor representation of the C_D data at the larger amplitudes. Also shown is Newtonian theory which overpredicts the drag at $\alpha = 0^\circ$ by about 60 percent.

To obtain a possibly more precise extrapolated value for C_D at $\alpha = 0^\circ$ (C_{D_o}), the data points below $\alpha_{rms} = 13^\circ$ were fitted in three different ways. The results are shown in figure 8. Again the filled symbols are not included in the least-squares fits. The Mach number 10 data, fitted alone, appear to have a slightly lower C_{D_o} and a faster rise with α_{rms} than the Mach number 26 data, fitted alone, or the all-data curve; however, caution should be used in interpreting this difference as a Mach number effect. A more striking feature is that the two data points below $\alpha = 2^\circ$ are low with respect to the quadratic fits through the data. This is not surprising considering that the flow separates over part of the flare and cylinder at $\alpha = 0^\circ$ and becomes fully attached on the windward meridian at $\alpha = 2^\circ$. Shown also are two calculated values for C_{D_o} - one obtained from embedded Newtonian theory (ref. 7) and one based on a separated-flow calculation. The separated-flow estimate is based on conical flow theory for the cone, Prandtl-Meyer expansion at the cone-cylinder junction, and oblique shock relationships through the shock waves where flow separation begins and where the flow reattaches on the flare. The separated-flow region is considered to be a solid surface or dead-air region with identical pressure to that behind the shock wave at the separation point on the cylinder (see sketch (b)). The geometric locations of separation

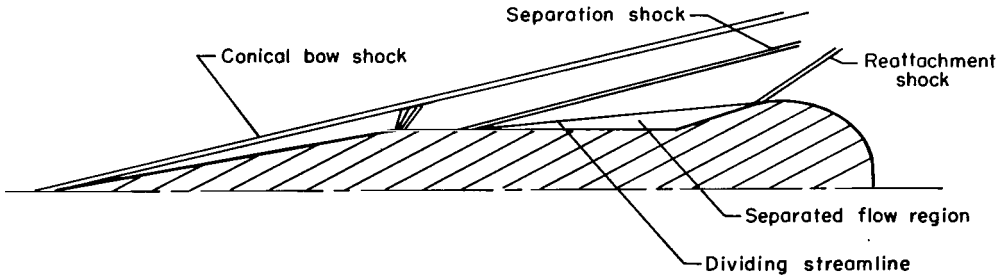

Sketch (b)

and reattachment points were measured from a shadowgraph of the model at $\alpha = 0^\circ$ and M = 10 (see fig. 4(a)). Skin-friction drag on the cone was included in the separated-flow drag estimate.

Static Stability - Nose-Forward Attitude

The quasilinear data for static stability, $C_{m_{\alpha_l}}$, both for M = 10 and 26 were considered as a group in deducing the pitching-moment-coefficient curve since there was no indication of Mach number effects either in the computed results or in the flow fields observed in the shadowgraphs. The quasilinear results are recorded in table I. All flights at M = 10 were divided as mentioned earlier, except four that either did not have enough cycles, or had

such small amplitudes that no improvement would result. None of the flights at $M = 26$ contained enough cycles to permit division into parts. The method of reference 5 was used to obtain a pitching-moment curve (explained in detail in appendix) and a plot of C_m versus α is shown in figure 9. Because of the high degree of nonlinearity over a wide angle-of-attack range, two separate polynomials were required to represent the pitching-moment characteristics adequately and the region of overlap is shown as the small area between the curves.

The static stability (represented by the local slope of the pitching-moment curve) is highest in the region of $\alpha = 0^\circ$ and then drops off rapidly to a minimum at $\alpha \sim 6^\circ$, where the stability begins to increase again and reaches a secondary maximum value in the vicinity of $\alpha = 12^\circ$ to 14°. This region of high stability at α near 12° correlates quite well with the previously discussed bow-shock impingement on the flare. The high stability at $\alpha = 0^\circ$ can be attributed to the separated laminar boundary layer over the cylinder and flare observed at low angles of attack. Reference 8 shows that laminar separation over flared bodies of revolution results in increased normal-force-curve slope and large rearward movements of centers of pressure. Similar results are presented in reference 9.

Newtonian theory is also shown for comparison. It considerably underestimates both the initial slope and the magnitude of the pitching-moment curve.

Static Stability - Nose-Rearward Attitude

Two flights were made for the purpose of determining pitching moments at angles of attack near 180°. Both flights were made at low-air densities to achieve as long a wavelength of oscillation as possible and thereby obtain a maximum number of shadowgraphs of the models in the attitude of interest. The low densities also resulted in Reynolds numbers that were in the range of interest for full-scale nose-rearward flight. It should be noted that both of the nose-rearward flights were nearly planar in nature with no measurable roll. The first flight was at $M = 7.82$ and $R = 0.0108 \times 10^6$. The resulting motion is shown in figure 10(a), where the variation of angle of attack with flight distance is plotted. As seen in the figure, the model oscillated to $\alpha_{max} = 165^\circ$ after a half cycle of motion from its attitude of 180° in the gun muzzle. The filled symbols were used to determine the equation of $\alpha = f(x)$. The actual maximum value of α and its location along the flight path were found first by least squares fitting the ten filled symbols with a fourth-degree polynomial in x and then setting the first derivative of the polynomial equal to zero. Two segments of the curve, one on each side of the maximum point, were then fitted by least squares with fourth-degree polynomials in x and differentiated twice to get $\alpha'' = f''(x)$. The pitching moments derived from these two segments were then plotted versus angle of attack and considered to be accurate over the range of angles of attack where the respective C_m values from the segments agreed reasonably well. They agreed within 2 percent from $\alpha = 165^\circ$ to 130°, so this was considered to be the region of confidence.

The second flight was made at the lowest density possible for the facility at $M = 9.2$ and a resulting $R = 0.0089 \times 10^6$. The motion experienced during this flight is seen in figure 10(b). The model rotated one complete revolution and passed through $\alpha = 180^\circ$ with a small α'. The filled symbols were used to obtain the desired pitching moment. The first objective was to determine the value of α' at $\alpha = 180^\circ$ and the corresponding value of x. This was done by least squares fitting a third-degree polynomial in x to the three points directly below and the two points directly above $\alpha = 180^\circ$. Once α' was determined, the procedure was essentially the same as for the previous test, except that the boundary value of α' was not equal to zero. The derived pitching moments from the two curves agreed very well from $\alpha = 180^\circ$ to 165°. The pitching-moment curve shown in figure 11, extending from $\alpha = 180^\circ$ to 130°, was derived from those two flights. The Newtonian theory prediction, also shown, compares favorably with the experimental result in this angle-of-attack range.

Construction of Entire Pitching-Moment Curve

With C_m determined experimentally over ranges of angles of attack near 0° and 180°, one could construct a reasonable C_m curve for the complete angle-of-attack range by choosing a theoretical value in the vicinity of $\alpha = 90^\circ$ to 100° (Newtonian value, for instance) and by extrapolating the experimental curves through the chosen point. However, it is possible to obtain a more precise definition of the pitching-moment curve near $\alpha = 100^\circ$ and, consequently, of the entire C_m curve, by an iterative technique in the following manner. An additional nose-rearward launch was made at $M = 7$ and $R = 0.165 \times 10^6$ in which the model oscillated through six cycles of motion, and damped from a maximum amplitude of 145° to 85°. (Ideally one would like to launch a model at an initial angle of $\alpha = 90^\circ$ to 100° and analyze the motion just as was done for the $\alpha = 180^\circ$ region, but model length prevented placing the model in the gun in this position.) The Reynolds number was higher than in the other two flights when the models were launched nose rearward because of the higher free-stream density necessary to produce more cycles of motion and because of the resultant damping to the amplitude range of interest. A synthetic motion, generated from numerical integration of the equations of free-flight motion, was matched to the observed motion using as inputs the flight conditions of the observed test (i.e., free-stream density and velocity history), the measured model characteristics, and the pitching-moment curves derived experimentally for the nose-forward and nose-rearward attitudes. (See ref. 10 for a complete derivation of the equations of motion and a description of the motion-synthesis program.) Starting values of pitching moment for angles of attack between 40° and 130° are determined by smooth extrapolation of the experimental data for nose-forward and nose-rearward attitudes to a value predicted by Newtonian theory for $\alpha = 100^\circ$ (see fig. 12). This estimated value and the resulting extrapolations were then altered by trial and error until the synthesized motion matched the observed motion. The constructed C_m curve was altered simply by raising or lowering the maximum point near $\alpha = 100^\circ$ and maintaining a smooth interpolation from each of the previously established curves. Figure 12 shows the final constructed curve for C_m versus α, as well as the Newtonian curve. Figure 13 shows the

synthetic motion and its relation to the data points from the observed motion. The value shown for $CMQ,(\xi - C_D)$, a modified dynamic-stability parameter (assumed constant for the entire angle range), is the final iterated value which in conjunction with the selected pitching-moment curve produces the best match to the observed amplitude change.

Figure 14 compares the observed data points and a motion generated with Newtonian pitching-moment coefficient. The match is seen to be poor, as the resulting frequency is somewhat low.

Dynamic Stability, Nose Forward

The dynamic-stability parameter ξ is plotted in figure 15 versus α_m, the average maximum amplitude in pitch, for each flight or flight segment. The model shows good dynamic stability throughout the angle range tested. Although several of the free-flight motions (including all flights at $M = 26$) are not adequate for defining dynamic stability accurately, the trend is for dynamic stability to decrease with increasing angle of attack. The models with "turbulent" flow (filled symbols) are slightly less stable dynamically than the models with laminar flow (open symbols). The large values of ξ, obtained for low angles of attack, may be strongly influenced by the nonlinear static stability, which increases rapidly as the angle of attack decreases, or they may simply indicate poor definition of amplitude in the small angle range where errors of tenths of a degree become significant.

CONCLUSIONS

Drag and stability characteristics and flow-field observations were obtained from free-flight tests of models of the slender flare-stabilized cone cylinder proposed by Goddard Space Flight Center for a Martian atmosphere probe. The results presented herein, for tests conducted in both a nose-forward and nose-rearward initial attitude, lead to the following conclusions:

1. Static stability decreases rapidly with increasing angle of attack until the bow-shock wave approaches the windward side of the flare. Further increase in angle of attack produces a notable increase in stability. The reduction in stability with increasing angle of attack at low angles was due, at least in part, to the observed laminar-boundary-layer separation over the cylinder and flare at low angles.

2. There are no significant differences in drag, stability, or flow-field characteristics between Mach numbers of 10 and 26 at a constant Reynolds number of 600,000; no effect of Reynolds number on drag or stability was measured at Reynolds numbers from 23,000 to 600,000 at a Mach number of 10.

3. The configuration is statically unstable in the nose-rearward attitude. The only stable trim point is at $\alpha = 0^{\circ}$ (nose forward).

4. The configuration is dynamically stable at all angles of attack.

Ames Research Center
National Aeronautics and Space Administration
Moffett Field, Calif., 94035, Jan. 20, 1967
124-07-02-13-00-21

APPENDIX A

METHOD OF OBTAINING NONLINEAR PITCHING-MOMENT CURVES FROM QUASILINEAR DATA

For a pitching-moment equation of the form of a polynomial,

$$-C_m = P_0\alpha + P_1\alpha^2 + P_2\alpha^3 + P_3\alpha^4 + P_4\alpha^5 + P_5\alpha^6 + P_6\alpha^7 \tag{A1}$$

the equation derived in reference 5 for the quasilinear value of the pitching-moment-curve slope can be written as

$$C_{m_{\alpha_l}} = P_0 a + \frac{8}{3} P_1 b + \frac{3}{4} P_2 c + \frac{8}{5} P_3 d + \frac{1}{12} P_4 e + \frac{8}{7} P_5 f + \frac{5}{32} P_6 g + \cdots \tag{A2}$$

where

$$a = 1$$

$$b = \frac{\frac{\alpha_m^5 + \alpha_{min}^5}{2} - \left(\frac{\alpha_m^2 + \alpha_{min}^2}{2}\right)^{5/2}}{(\alpha_m^2 - \alpha_{min}^2)^2}$$

$$c = \alpha_m^2 + \alpha_{min}^2$$

$$d = \frac{\frac{\alpha_m^7 + \alpha_{min}^7}{2} - \left(\frac{\alpha_m^2 + \alpha_{min}^2}{2}\right)^{7/2}}{(\alpha_m^2 - \alpha_{min}^2)^2}$$

$$e = 7\alpha_m^4 + 10\alpha_m^2\,\alpha_{min}^2 + 7\alpha_{min}^4$$

$$f = \frac{\frac{\alpha_m^9 + \alpha_{min}^9}{2} - \left(\frac{\alpha_m^2 + \alpha_{min}^2}{2}\right)^{9/2}}{(\alpha_m^2 - \alpha_{min}^2)^2}$$

$$g = 3\alpha_m^6 + 5\alpha_m^4\,\alpha_{min}^2 + 5\alpha_m^2\,\alpha_{min}^4 + 3\alpha_{min}^6$$

A computer program was developed for applying these equations. It uses the method of least squares, considers all possible polynomials with from two to five of the seven terms shown in equation (A1), and selects the one polynomial from each of these four classes of polynomials (i.e., two, three, four,

or five terms) that produces the best fit to the $C_{m_{\alpha_l}}$, α_m, and α_{min} data. The class of polynomials judged to be the most representative of the data is then chosen. (The best five-term polynomials will always be a better fit than the best four-term polynomials, for example, but may not be a reasonable representation of the data. For example, a five term polynomial could be made to fit five data points exactly, but the resulting curve might have such large variations between points that it would be completely useless. A three- or four-term polynomial, on the other hand, might prevent these large variations and be a more reasonable curve even though it can not pass through each point exactly.) With the coefficients P_0, P_1, P_2, etc., determined, the pitching-moment coefficient is expressed by equation (A1), where some values of P will be omitted, depending on the number and degree of terms.

Figure 16 illustrates the application of this procedure to the present data. From the variation of the apparent static stability with angle of attack, it is obvious that the static stability is not linear. It can be seen from equation (A2) that if $\alpha_{min} \neq 0$ and the pitching-moment slope is not linear, there is no exact form for plotting $C_{m_{\alpha_l}}$ directly on a two-dimensional plot (three dimensions are required). For most test motions, however, α_{min} is much smaller than α_m and an approximate representation of the data (such as fig. 16) can be shown by plotting $C_{m_{\alpha_l}}$ versus α_m from equation (A1), where α_{min} is set equal to zero. Because the variation of the data with α_m was not simple, two separate polynomials were necessary to represent the data adequately. These two curves in their approximate form (approximate because α_{min} has been set equal to zero) overlap in the vicinity of $\alpha_m = 15^\circ$. These two polynomials produce the two polynomials describing $C_m = C_m(\alpha)$ shown in figure 9.

REFERENCES

1. Allen, H. Julian: Motion of a Ballistic Missile Angularly Misaligned With the Flight Path Upon Entering the Atmosphere, and Its Effect Upon Aerodynamic Heating, Aerodynamic Loads, and Miss Distance. NACA TN 4048, 1957.

2. Nicolaides, John D.: On the Free-Flight Motion of Missiles Having Slight Configurational Asymmetries. Rep. 858, BRL, Aberdeen Proving Ground, 1953.

3. Sommer, Simon C.; Short, Barbara J.; and Compton, Dale L.: Free-Flight Measurements of Static and Dynamic Stability of Models of the Project Mercury Re-entry Capsule at Mach Numbers 3 and 9.5. NASA TM X-373, 1960.

4. Short, Barbara J.; and Sommer, Simon C.: Some Measurements of the Dynamic and Static Stability of Two Blunt-Nosed, Low-Fineness-Ratio Bodies of Revolution in Free Flight at M= 4. NASA TM X-20, 1959.

5. Rasmussen, Maurice L.; and Kirk, Donn B.: On the Pitching and Yawing Motion of a Spinning Symmetric Missile Governed by an Arbitrary Non-linear Restoring Moment. NASA TN D-2135, 1964.

6. Seiff, Alvin: A New Method for Computing Drag Coefficients From Ballistic-Range Data. J. Aero. Sci., vol. 25, no. 2, Feb. 1958, pp. 133-134.

7. Seiff, Alvin: Secondary Flow Fields Embedded in Hypersonic Shock Layers. NASA TN D-1304, 1962.

8. Dennis, David H.: The Effects of Boundary-Layer Separation Over Bodies of Revolution With Conical Tail Flares. NACA RM A57I30, 1957.

9. Short, Barbara J.; Whiting, Ellis E.; Kruse, Robert L.; and Malcolm, Gerald N.: A Comparison of the Hypersonic Static-Stability Characteristics of Blunt- and Pointed-Nosed Slender Entry Vehicles. NASA TM X-850, 1963.

10. Malcolm, Gerald N.; and Kirk, Donn B.: Comparison of Free-Flight and Conventional Wind-Tunnel Stability Tests for Apollo Command Module and Abort Configurations. NASA TM X-1137, 1965.

TABLE I.- MODEL CHARACTERISTICS AND TEST CONDITIONS

Test (a)	M	$R \times 10^{-6}$	V, m/sec	ρ, kg/m^3	α_m, deg	α_{min}, deg	α_{rms}, deg	C_D	$-C_{m_{\alpha_\zeta}}$	$-\xi$	m, gm	d, cm	$\frac{X_{cg}}{d}$	$I \times 10^8$, $kg\text{-}m^2$	$\left(\frac{d}{\sigma}\right)^2$	Facility (b)
[c]1463	9.87	0.606	3378.7	0.6360			4.30	0.144			1.1407	0.5098	2.369	3.38	0.876	PHFFF
[c]1463-1	9.89	.607	3385.4	.6360	6.49	0.23			1.847	7.3	1.1407	.5098	2.369	3.38	.876	PHFFF
[c]1463-2	9.85	.605	3372.0	.6360	5.98	.24			1.950	3.6	1.1407	.5098	2.369	3.38	.876	PHFFF
[c]1594	10.38	.632	3554.0	.6329	2.12	.99	1.63	.102	2.627	20.9	1.1453	.5080	2.400	3.46	.855	PHFFF
885	10.42	.0231	3513.1	.02288	31.34	1.93	22.96	.850	1.793	20.8	1.1267	.5075	2.376	3.28	.884	PBR
1521	9.76	.148	3362.5	.1578	16.08	.98	10.66		1.597		1.2052	.5085	2.424	3.44	.904	PHFFF
1542-1	9.97	.601	3432.3	.6272	7.00	.20	4.98	.136	1.415	28.2	1.1647	.5093	2.389	3.44	.876	PHFFF
1542-2	9.94	.599	3421.7	.6272	4.61	.28	3.04	.111	1.866	55.2	1.1647	.5093	2.389	3.44	.876	PHFFF
1668	10.22	.603	3544.2	.6194	2.35	.35			3.090	73.2	1.1607	.5070	2.387	3.34	.894	PHFFF
1668-1	10.23	.604	3547.9	.6194			1.79	.093			1.1607	.5070	2.387	3.34	.894	PHFFF
1668-2	10.21	.603	3540.2	.6194			.88	.079			1.1607	.5070	2.387	3.34	.894	PHFFF
1669-1	10.45	.632	3597.8	.6282	5.80	1.05	4.23	.122	1.779	7.4	1.1808	.5105	2.378	3.37	.914	PHFFF
1669-2	10.42	.631	3588.4	.6282	5.06	.74	3.60	.113	1.936	12.2	1.1808	.5105	2.378	3.37	.914	PHFFF
1671-1	10.31	.573	3584.1	.5832	5.32	2.32	4.08	.130	1.837	3.8	1.2045	.5065	2.428	3.43	.901	PHFFF
1671-2	10.29	.571	3573.2	.5832	4.77	1.93	3.63	.128	1.852	6.4	1.2045	.5065	2.428	3.43	.901	PHFFF
1672-1	10.39	.563	3657.0	.5690	9.22	.21	6.21	.158	1.570	8.3	1.1698	.5098	2.387	3.40	.896	PHFFF
1672-2	10.37	.561	3648.1	.5690	8.79	.48	6.36	.156	1.564	8.4	1.1698	.5098	2.387	3.40	.896	PHFFF
1673-1	10.38	.578	3516.2	.5934	46.71	5.10	32.69	1.235	1.555	7.7	1.1757	.5108	2.368	3.43	.894	PHFFF
1673-2	9.87	.564	3421.7	.5934	38.75	3.80	26.72	.990	1.688	9.8	1.1757	.5108	2.368	3.43	.894	PHFFF
1547	26.7	.552	5197.0	.1382	9.82	2.15	6.87	.154	1.007	17.5	1.1906	.5080	2.418	3.39	.906	PHFFF
1548	26.7	.614	5266.0	.1534	12.14	2.50	8.58	.186	1.430	10.1	1.1888	.5126	2.379	3.46	.903	PHFFF
1549	25.6	.613	5100.0	.1621	15.35	.11	10.46	.235	1.563	16.2	1.1718	.5105	2.385	3.35	.911	PHFFF
1550	26.2	.626	5225.0	.1618	15.69	1.93	11.21	.243	1.398	24.9	1.1650	.5093	2.371	3.31	.913	PHFFF
1551	26.0	.625	5186.0	.1629	18.84	1.04	12.90	.305	1.750	7.2	1.1795	.5105	2.380	3.43	.896	PHFFF
1552	26.2	.666	5225.0	.1720	13.80	1.04	9.47	.220	1.360	30.4	1.1802	.5118	2.387	3.43	.900	PHFFF
[d]842	7.03	.165	2376.5	.2422							1.1436	.5088	2.377	3.34	.887	PBR
[d]974	7.83	.0107	2652.0	.01422							1.1321	.5095	2.371	3.36	.874	PBR
[d]975	9.22	.00889	3144.9	.009947							1.1570	.5105	2.383	3.39	.890	PBR

[a]The numerals 1 and 2 following test numbers indicate first or second segment of a complete flight that has been split into two separate parts for analysis. (Explanation in section on data-reduction method.) Test 1463 was split for stability data but not for drag. Test 1668 was split for drag but not for stability.

[b]PHFFF - Prototype Hypervelocity Free-Flight Facility; PBR - Pressurized Ballistic Range.

[c]Models with "turbulent" flow.

[d]Models launched in nose-rearward position.

Note: Blanks indicate parameter is not applicable for that flight or flight segment.

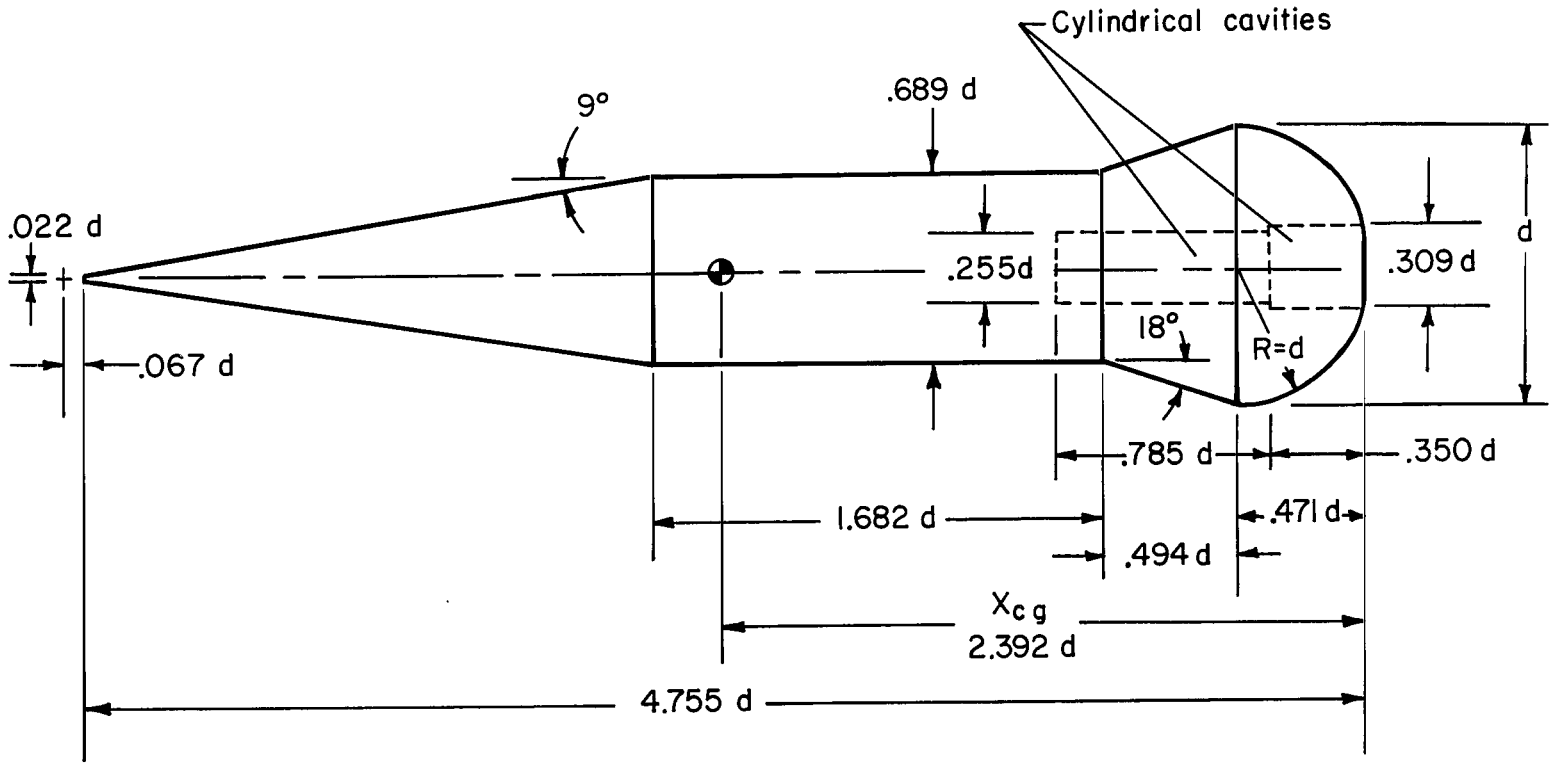

Figure 1.- Sketch of model.

A-37592

Figure 2.- Models and sabots.

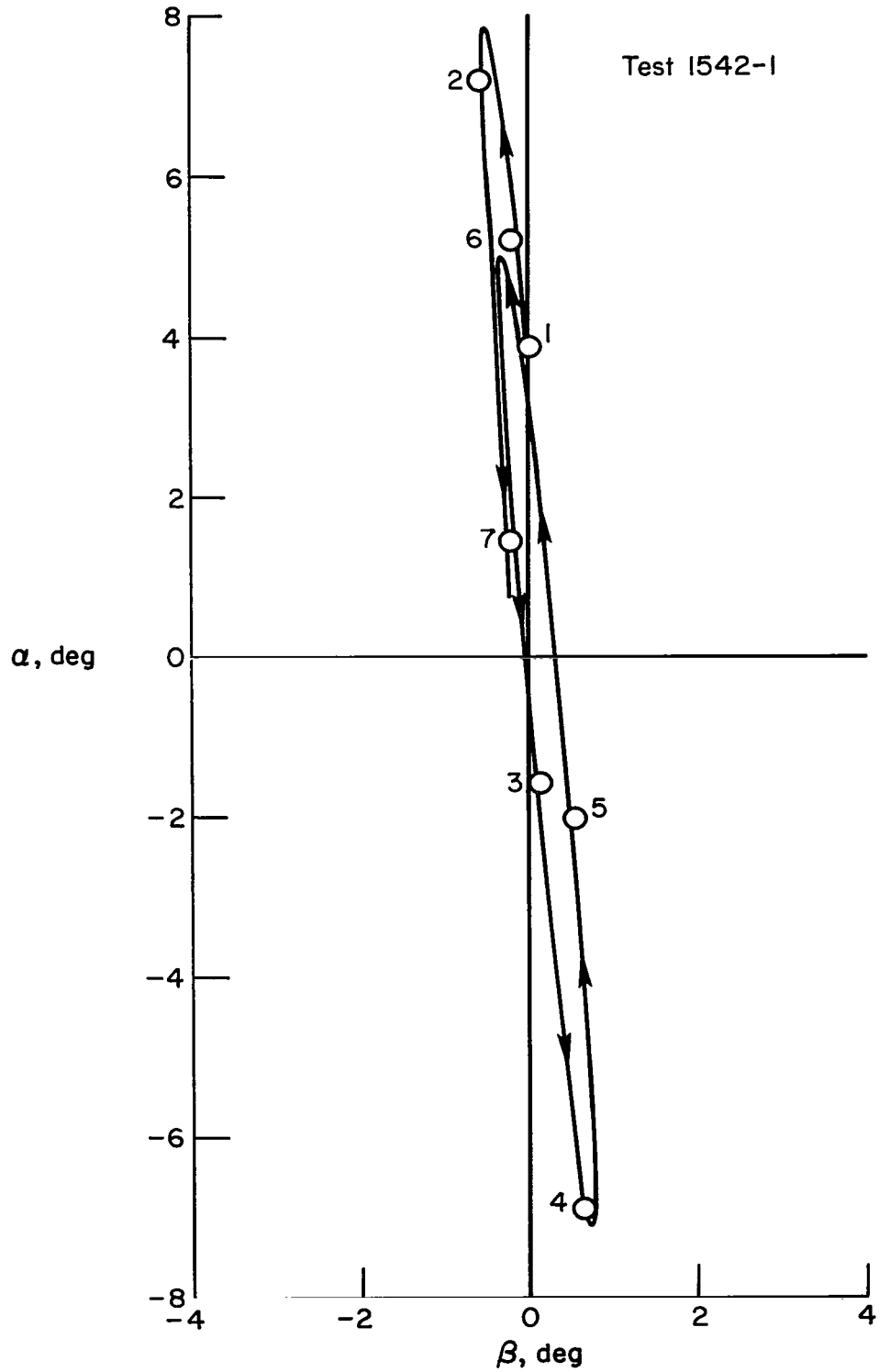

(a) Near-planar motion.

Figure 3.- Typical pitch-yaw motions.

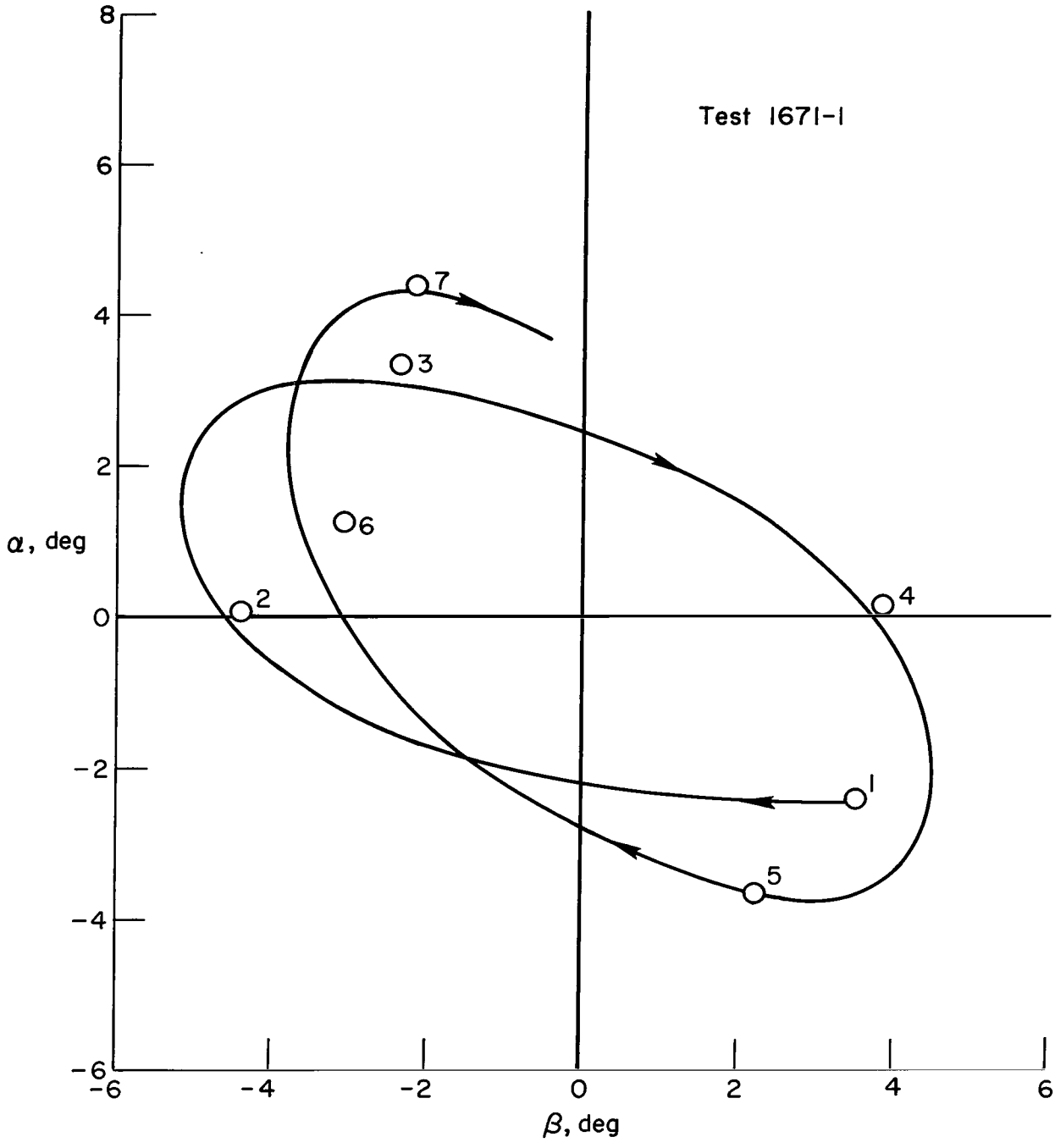

(b) Open precessing motion.

Figure 3.- Concluded.

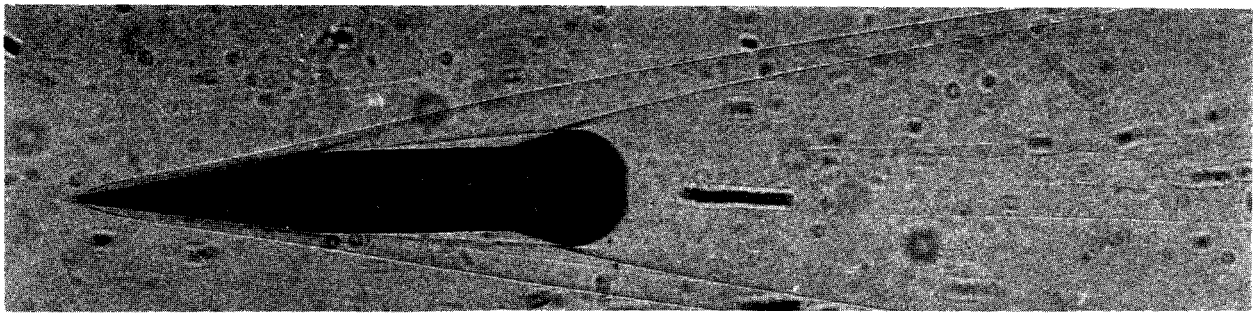

$\alpha = 0.0^{\circ}$ ($\beta = 0.7^{\circ}$), M = 9.92, R = 0.598×10^{6} A-36957-1

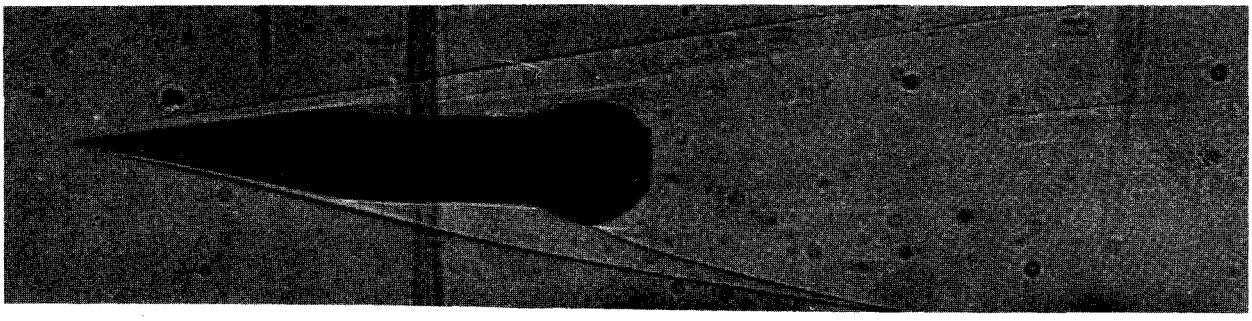

$\alpha = 1.3^{\circ}$ ($\beta = -0.6^{\circ}$), M = 9.94, R = 0.599×10^{6} A-36957-2

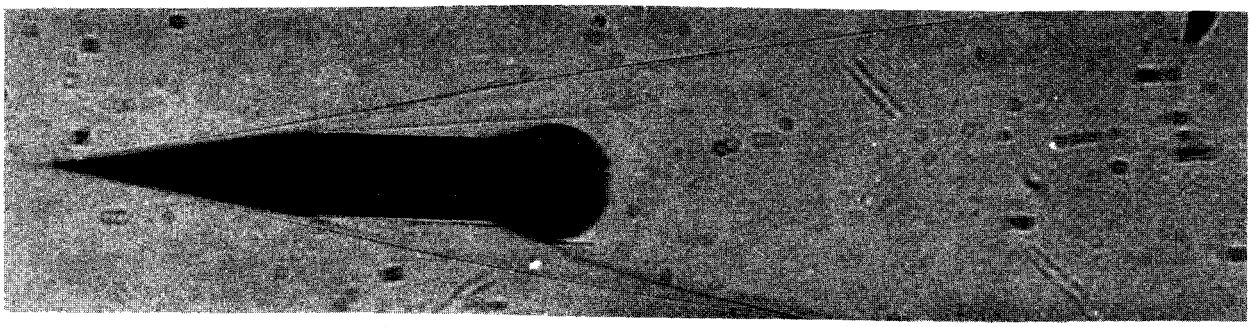

$\alpha = 1.6^{\circ}$ ($\beta = -0.2^{\circ}$), M = 9.99, R = 0.602×10^{6} A-36957-3

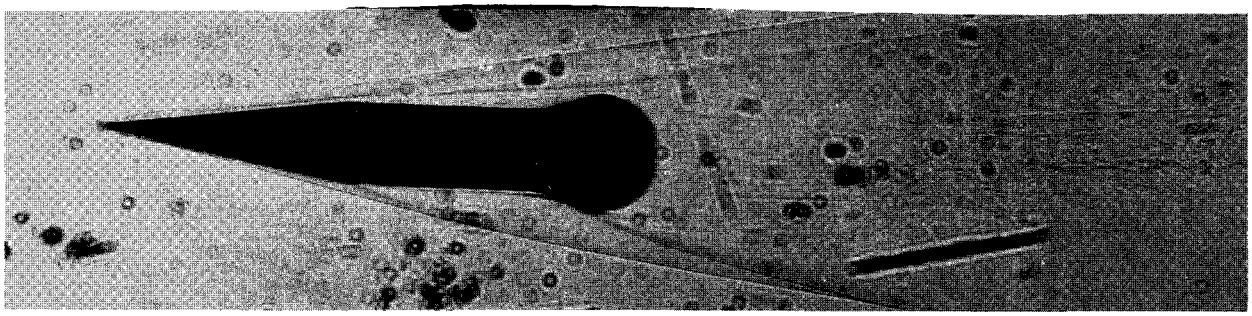

$\alpha = 2.0^{\circ}$ ($\beta = -0.6^{\circ}$), M = 9.97, R = 0.600×10^{6} A-36957-4

(a) Test 1542, tantalum-tungsten alloy nose.

Figure 4.- Shadowgraphs of model in flight at M = 10.

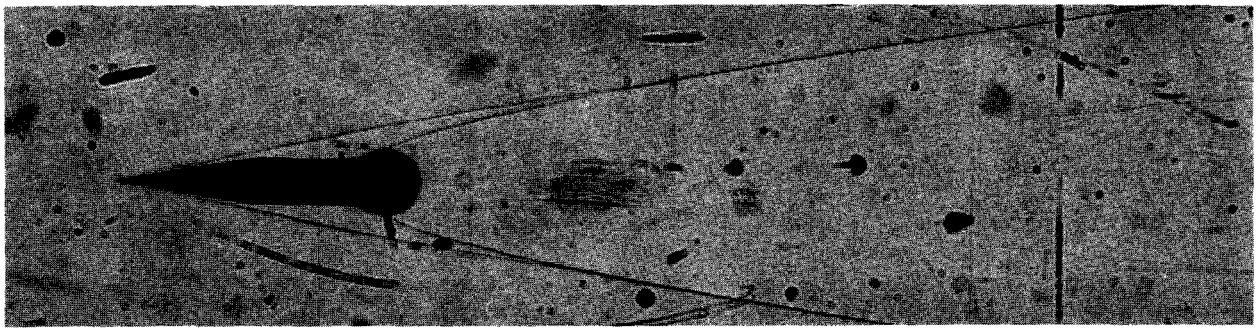

$\alpha = 0.8^{\circ}$ ($\beta = -5.0^{\circ}$), M = 9.92, R = 0.609×10^{6} A-34745

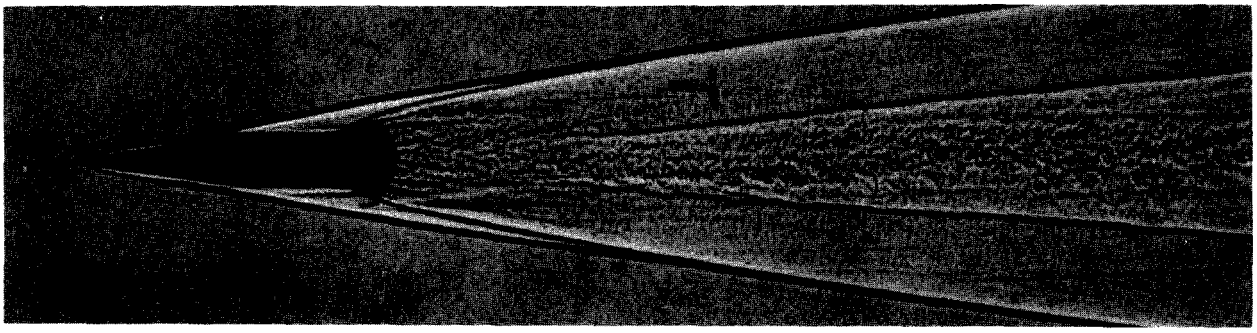

$\alpha = -0.6^{\circ}$ ($\beta = 0.0^{\circ}$), M = 9.82, R = 0.603×10^{6} A-34744

(b) Test 1463, sintered tungsten-iron-nickel nose.

Figure 4.- Concluded.

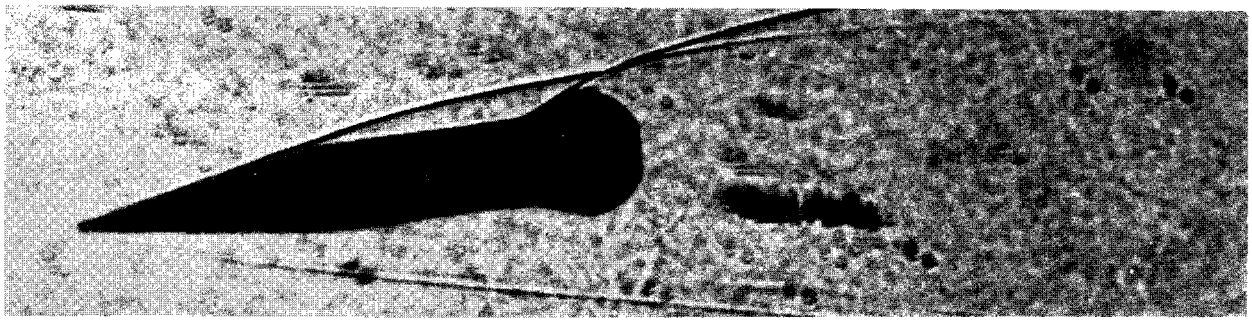

$\alpha = -8.5^{\circ}$ ($\beta = 1.3^{\circ}$), M = 26.2, R = 0.672×10^{6} A-36957-5

$\alpha = -10.6^{\circ}$ ($\beta = -1.0^{\circ}$), M = 26.2, R = 0.670×10^{6} A-36957-6

$\alpha = -11.9^{\circ}$ ($\beta = 1.3^{\circ}$), M = 26.3, R = 0.626×10^{6} A-36957-7

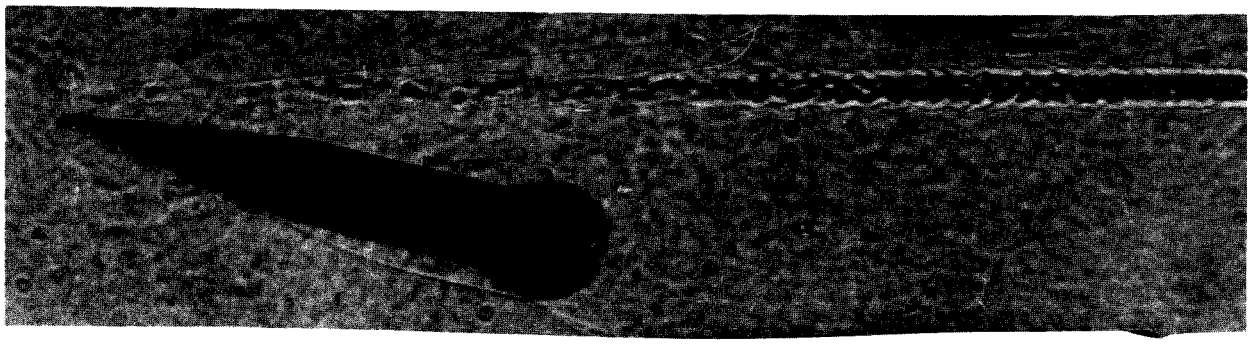

$\alpha = 14.2^{\circ}$ ($\beta = 0.8^{\circ}$), M = 26.2, R = 0.672×10^{6} A-36957-8

Figure 5.- Shadowgraphs of model at M = 26 at various angles of attack.

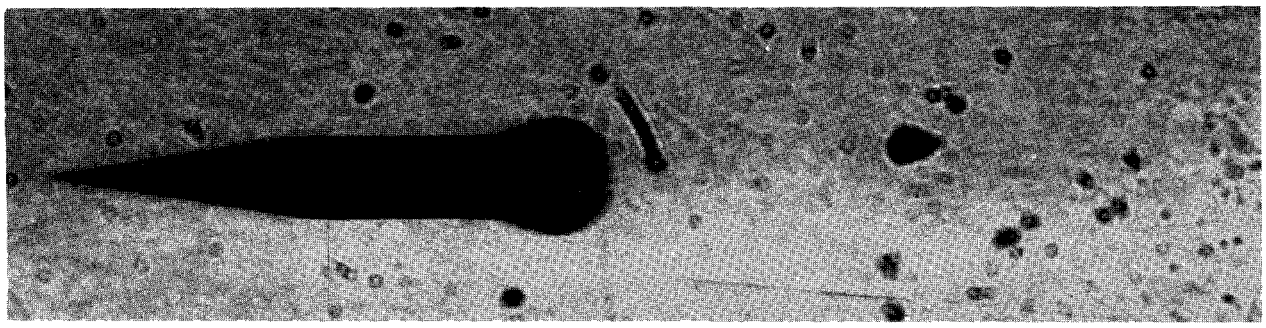

$\alpha = 0.0^{\circ}$ ($\beta = -0.9^{\circ}$), M = 26.1, R = 0.628×10^{6} A-36957-9

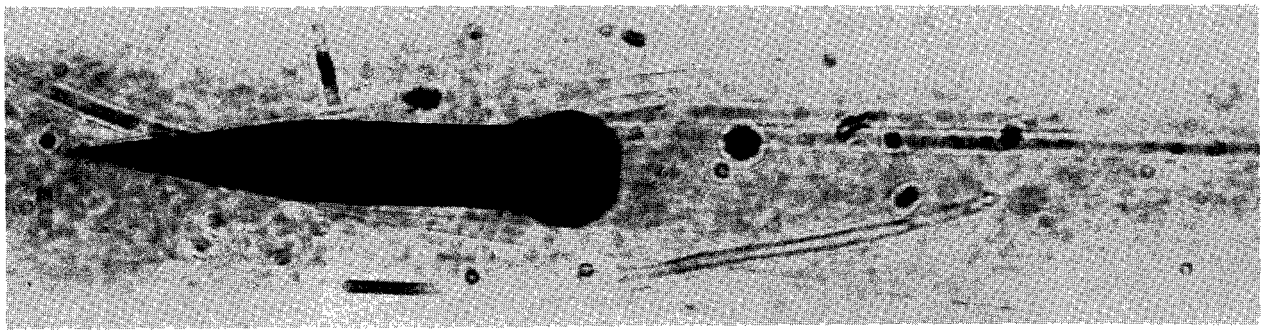

$\alpha = 0.9^{\circ}$ ($\beta = 0.0^{\circ}$), M = 26.1, R = 0.628×10^{6} A-36957-10

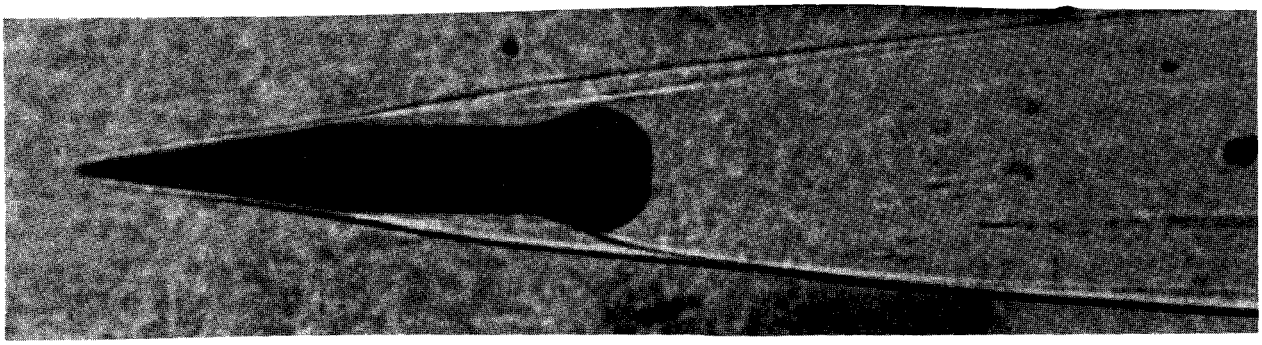

$\alpha = 1.4^{\circ}$ ($\beta = 2.0^{\circ}$, M = 26.0, R = 0.627×10^{6} A-36957-11

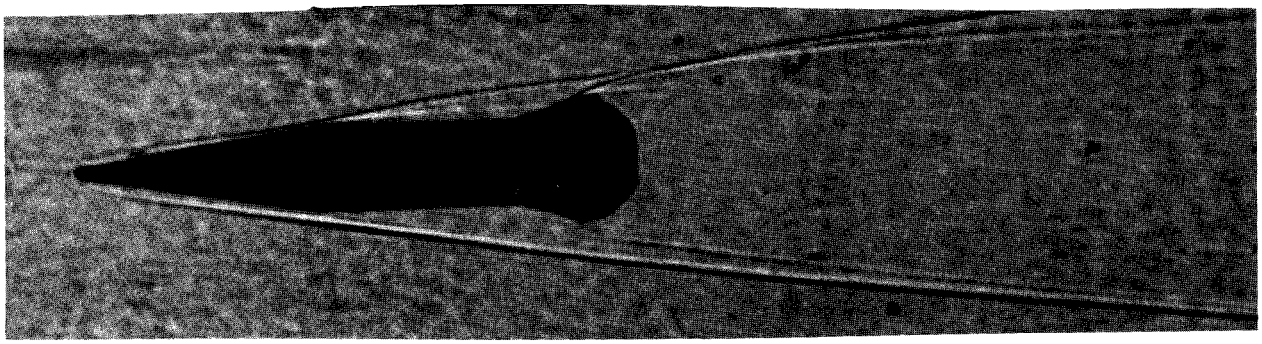

$\alpha = -2.0^{\circ}$ ($\beta = -1.3^{\circ}$), M = 26.2, R = 0.670×10^{6} A-36957-14

Figure 6.- Shadowgraphs of model at M = 26 at low angles of attack.

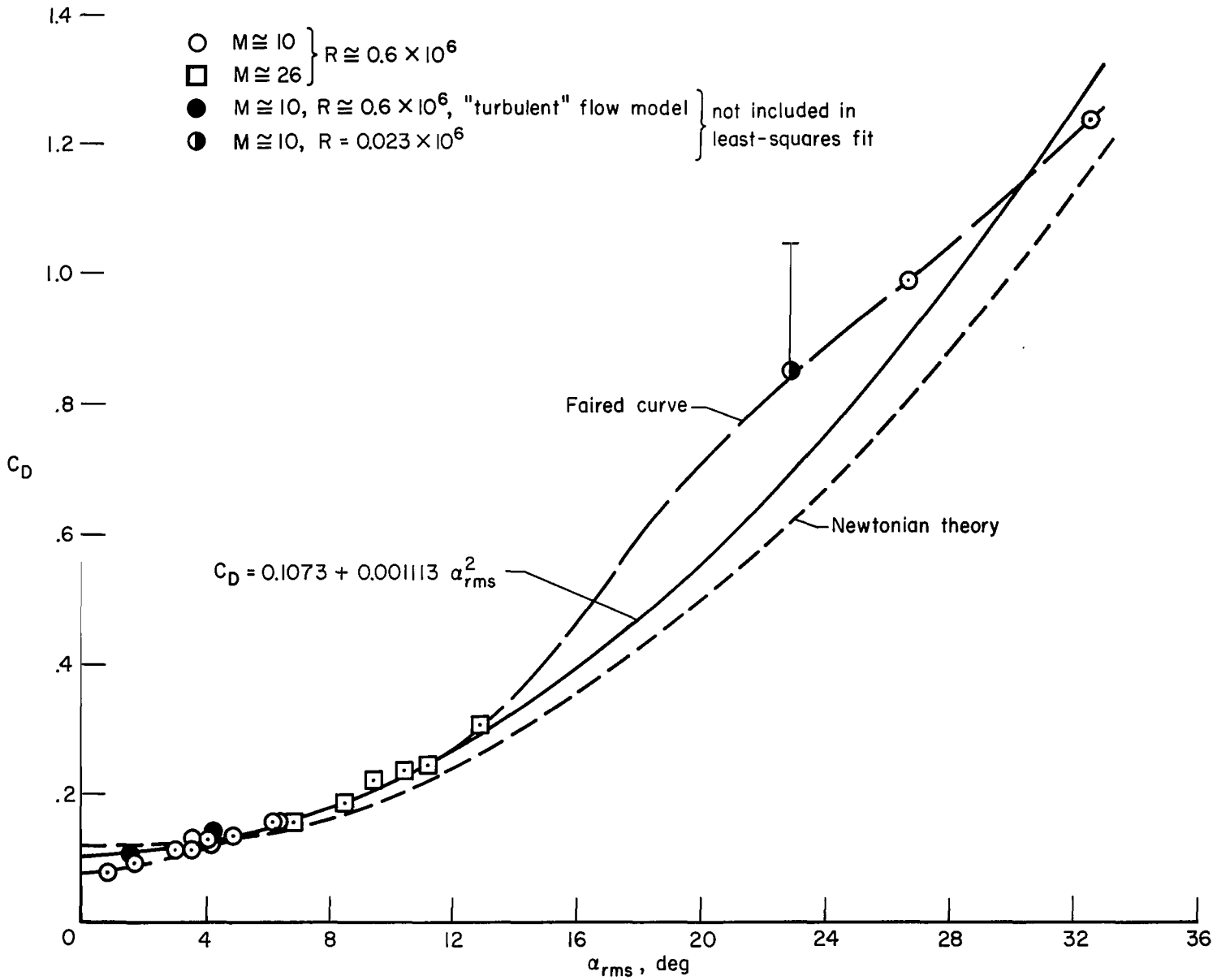

Figure 7.- Variation of drag coefficient with α_{rms}.

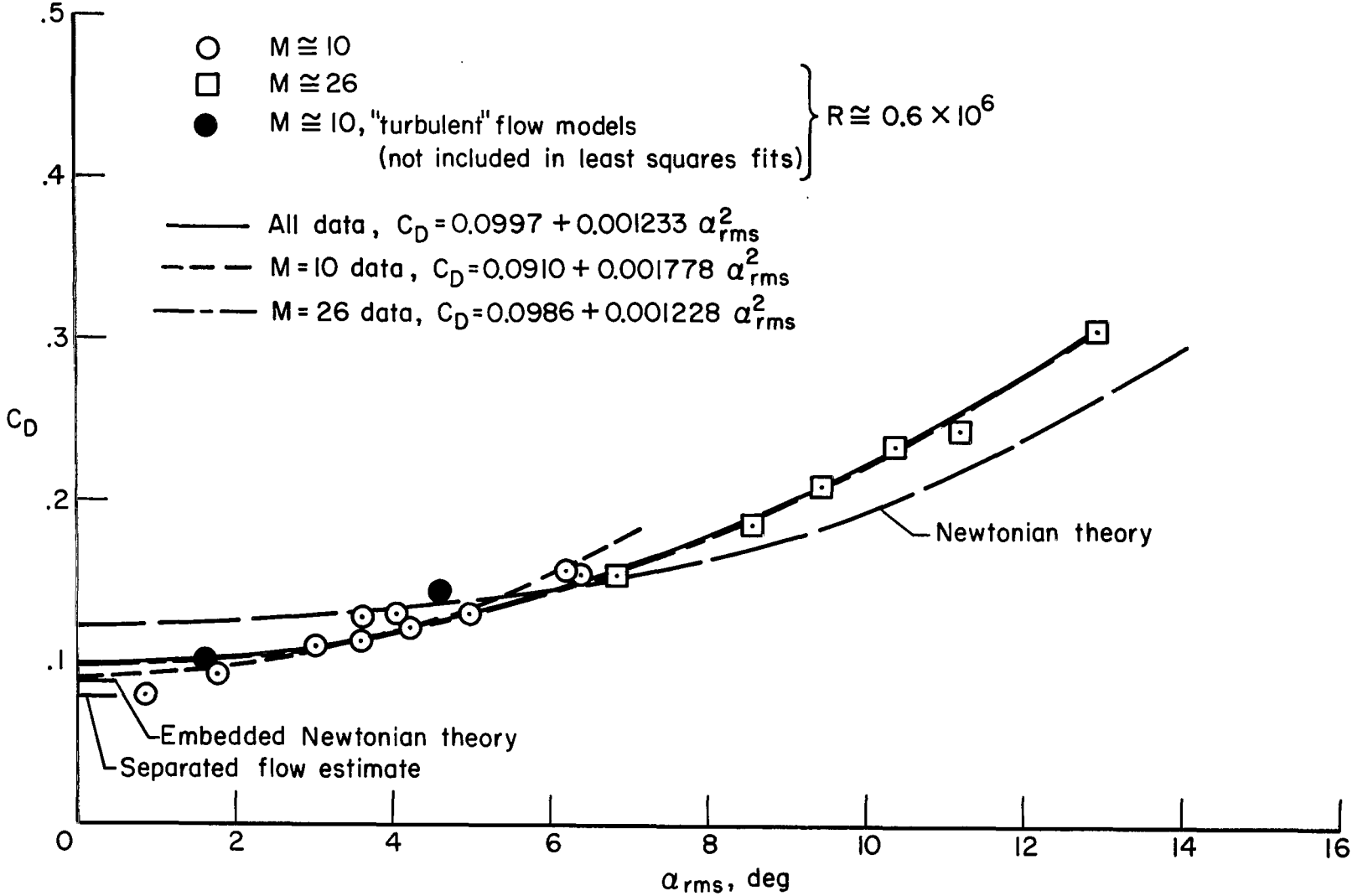

Figure 8.- Variation of drag coefficient with α_{rms} and estimate of C_{D_o}.

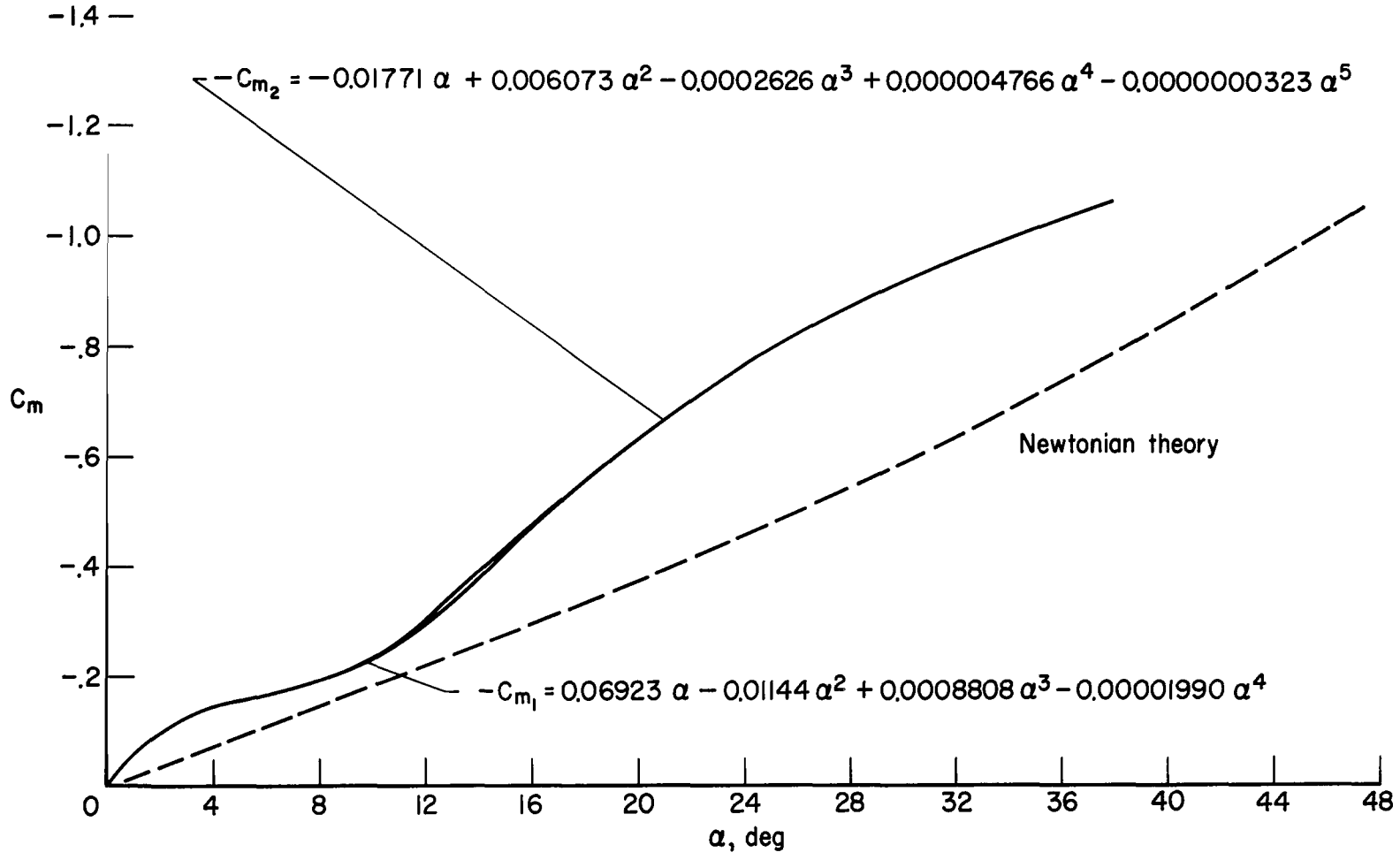

Figure 9.- Pitching-moment coefficient, nose-forward attitude.

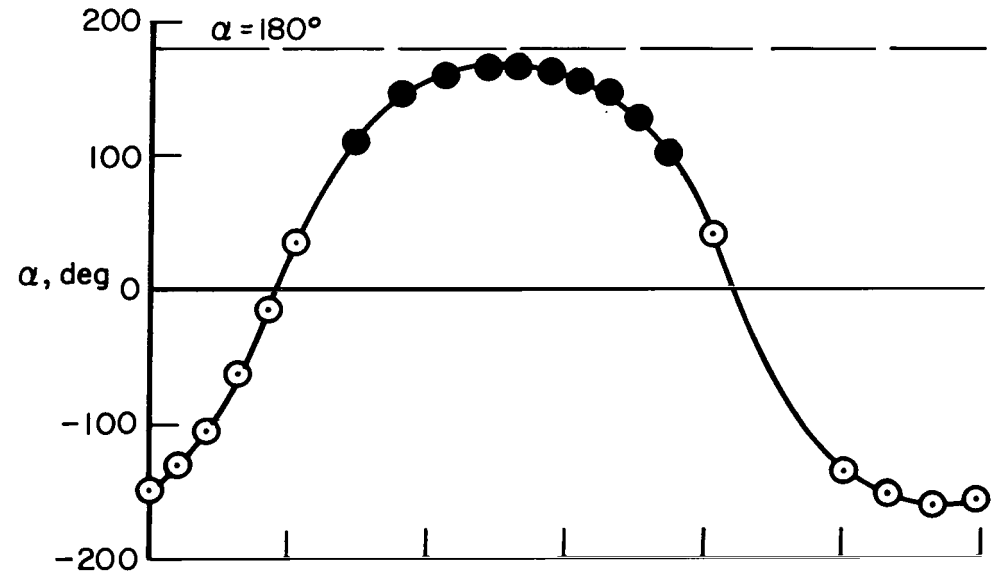

(a) Test 974.

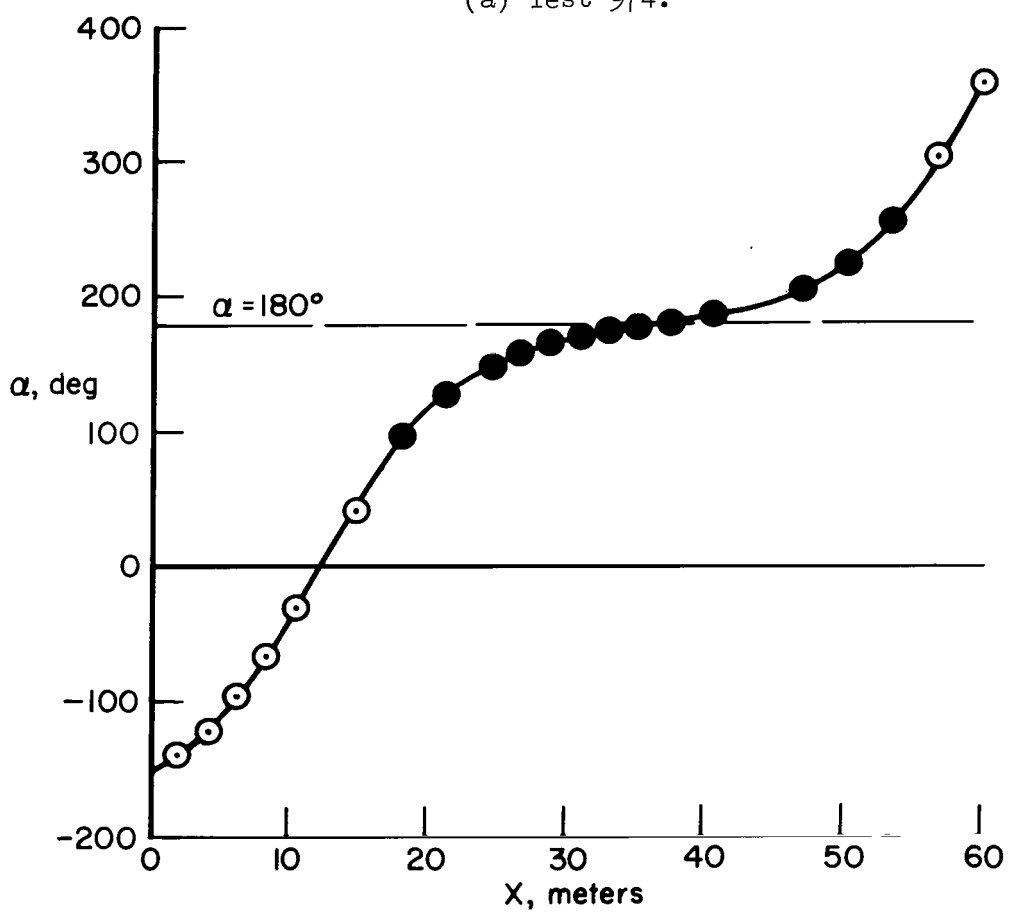

(b) Test 975.

Figure 10.- Angle-of-attack history for nose-rearward flights.

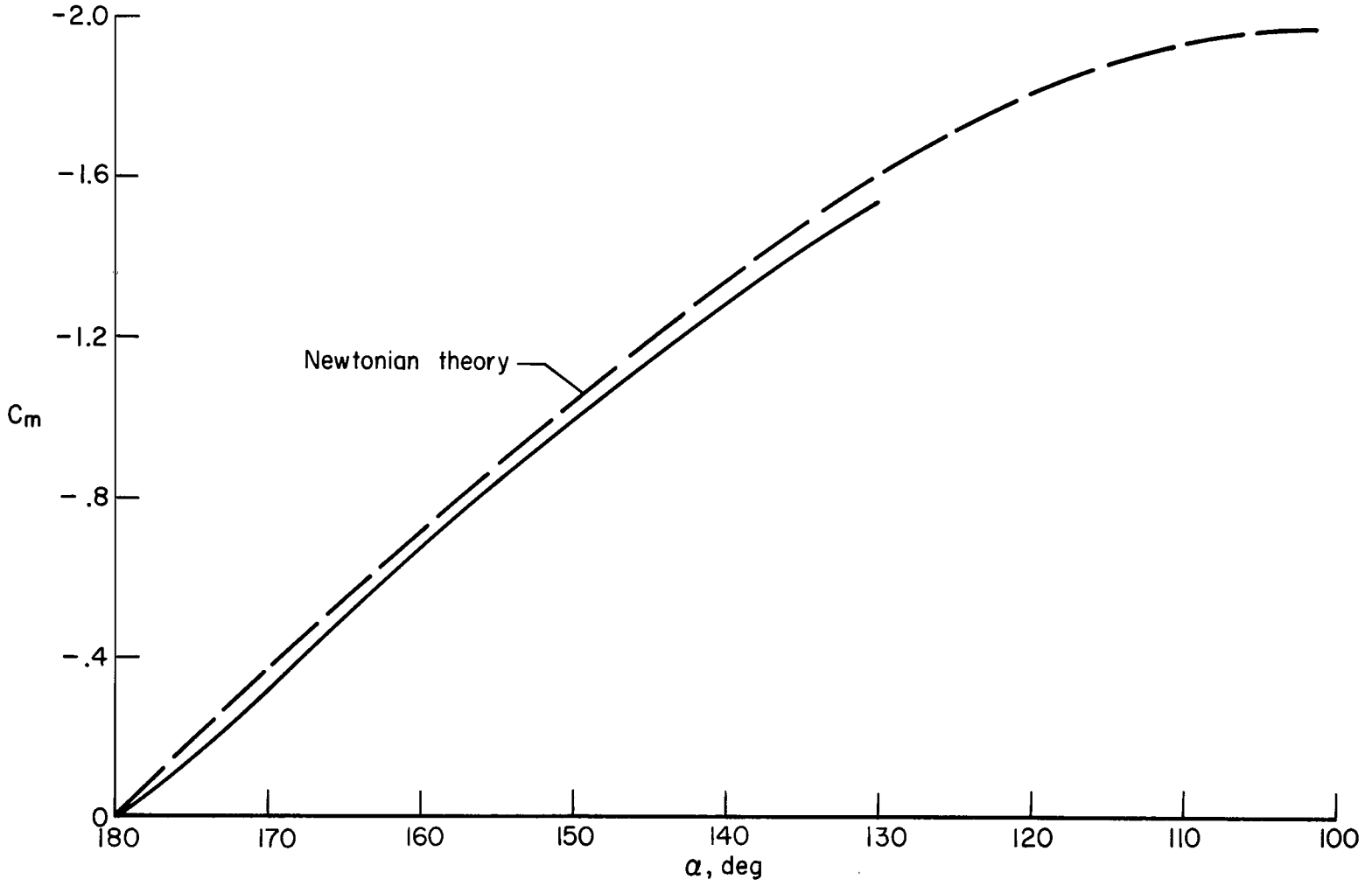

Figure 11.- Pitching-moment coefficient, nose-rearward attitude.

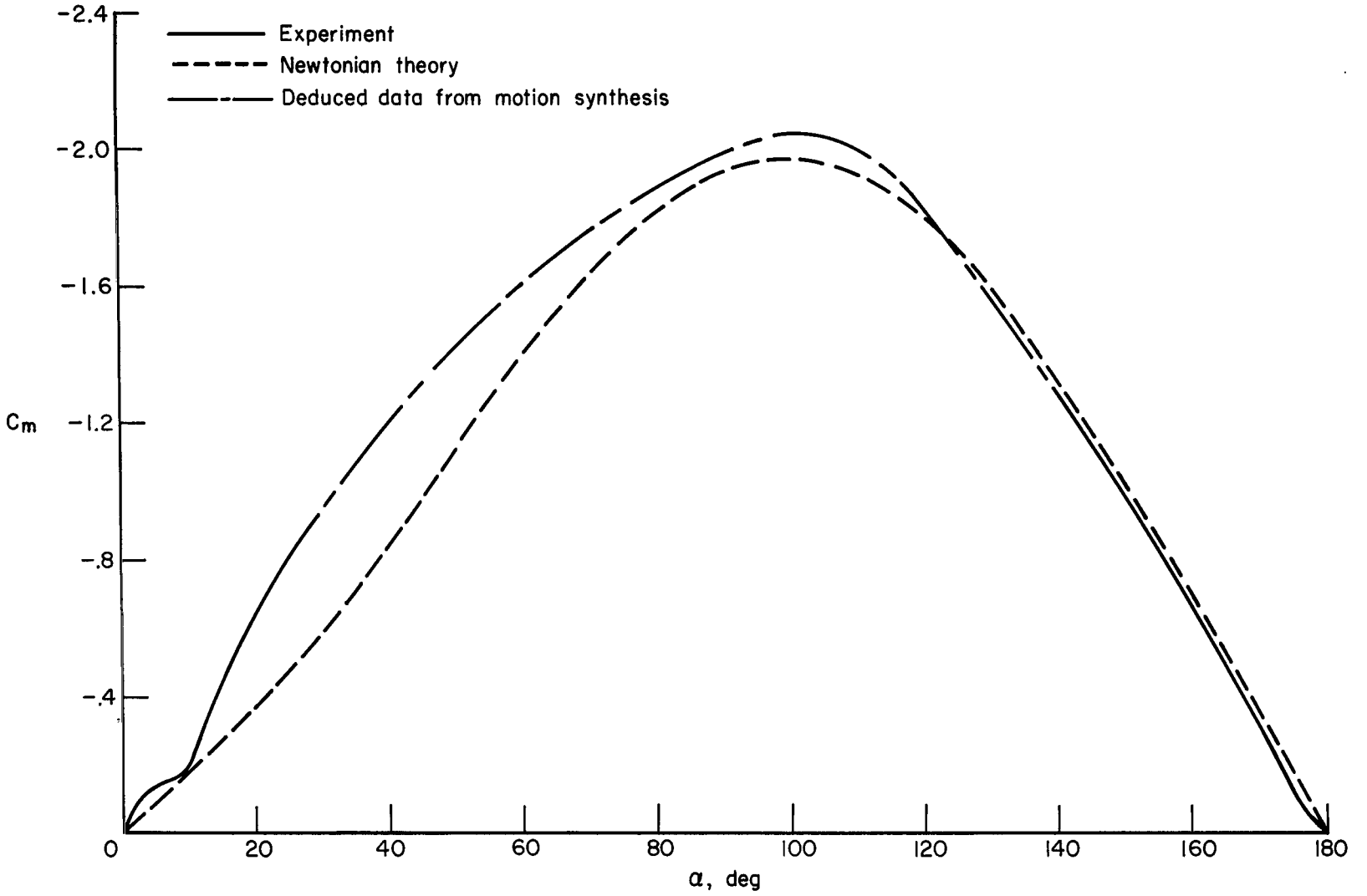

Figure 12.- Variation of pitching-moment coefficient with angle of attack.

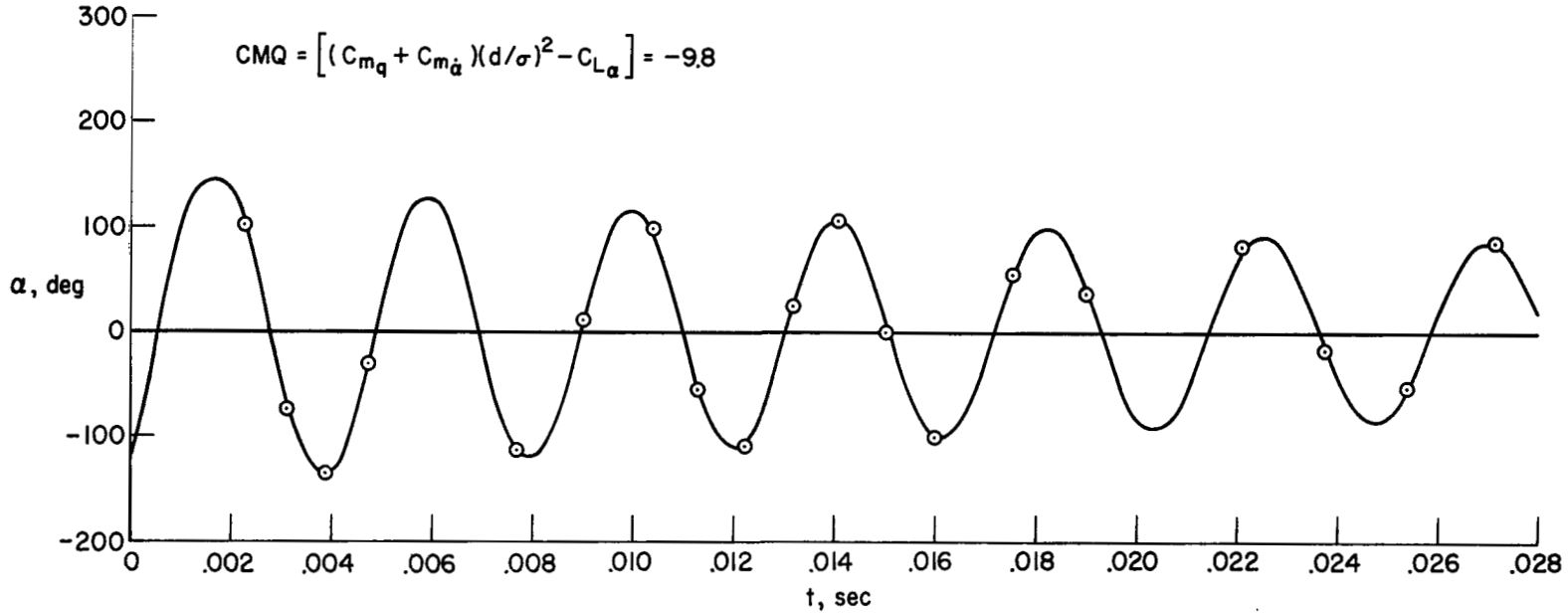

Figure 13.- Comparison of observed data points (test 842) and motion synthesized with experimental C_m curve.

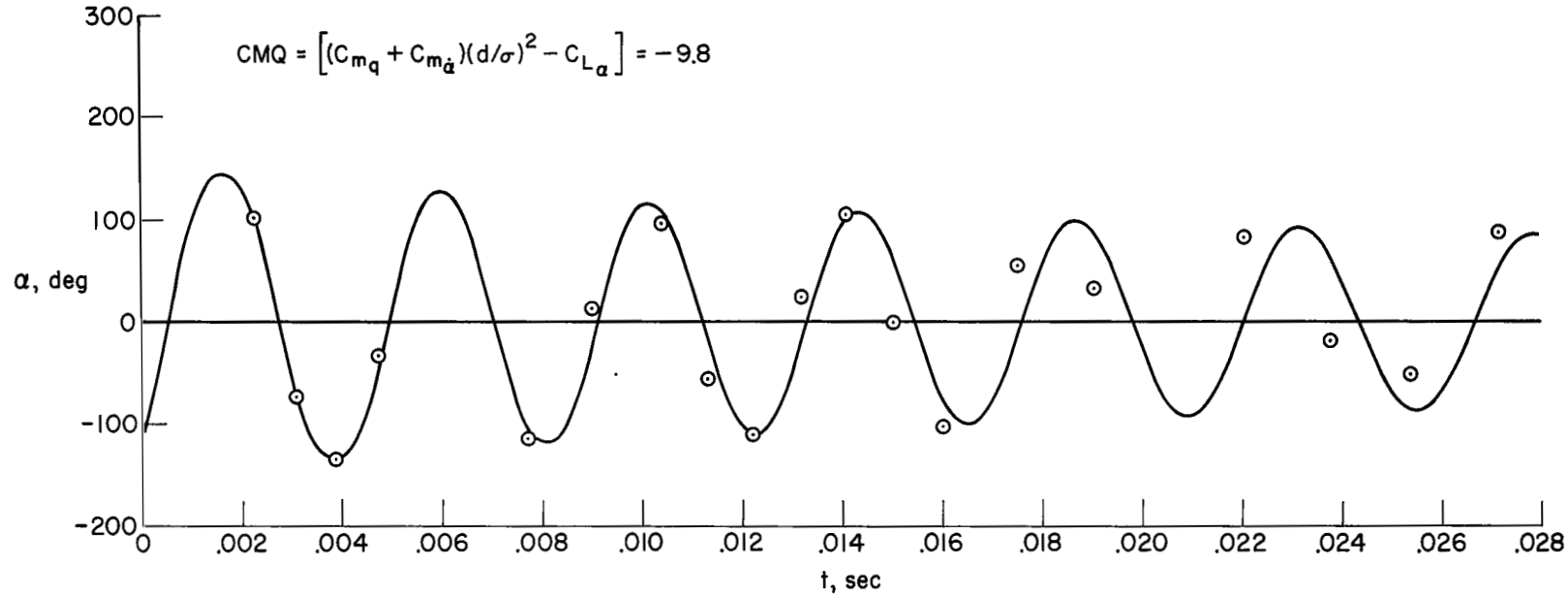

Figure 14.- Comparison of observed data points (test 842) and motion synthesized with Newtonian C_m curve.

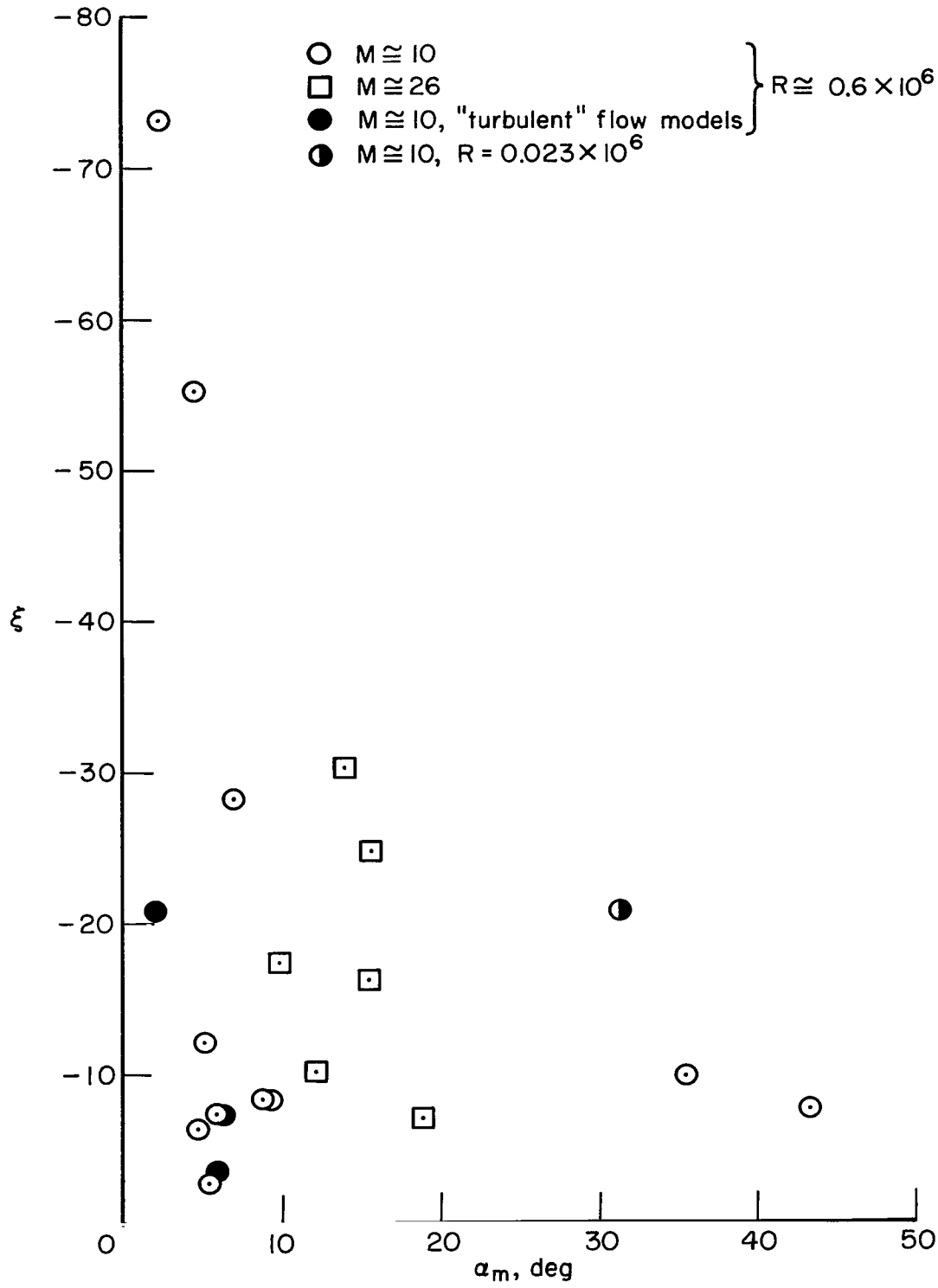

Figure 15.- Variation of dynamic-stability parameter with average maximum amplitude of oscillation.

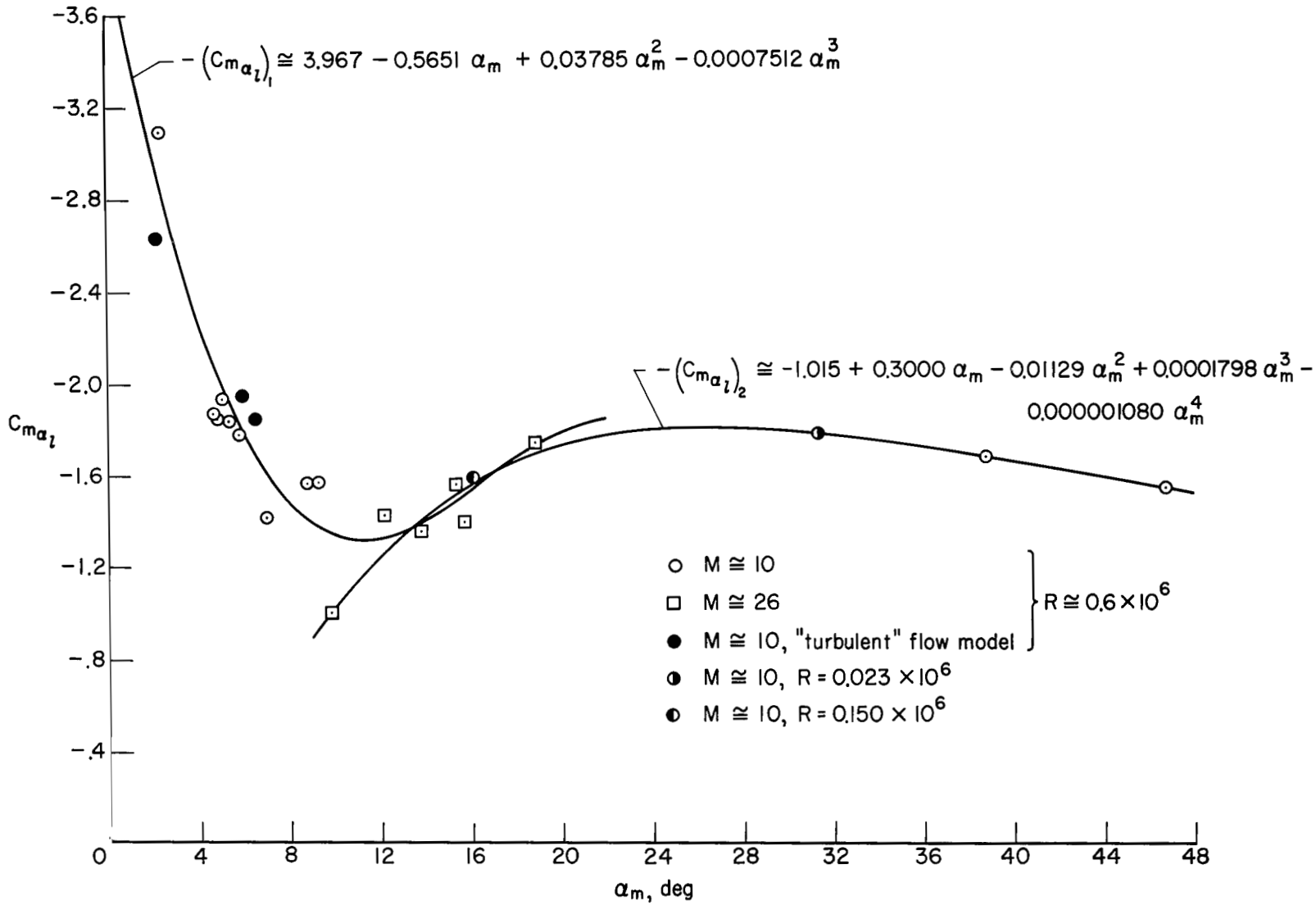

Figure 16.- Variation of quasilinear pitching-moment curve slope with average maximum amplitude of oscillation.

"The aeronautical and space activities of the United States shall be conducted so as to contribute . . . to the expansion of human knowledge of phenomena in the atmosphere and space. The Administration shall provide for the widest practicable and appropriate dissemination of information concerning its activities and the results thereof."

—NATIONAL AERONAUTICS AND SPACE ACT OF 1958

NASA SCIENTIFIC AND TECHNICAL PUBLICATIONS

TECHNICAL REPORTS: Scientific and technical information considered important, complete, and a lasting contribution to existing knowledge.

TECHNICAL NOTES: Information less broad in scope but nevertheless of importance as a contribution to existing knowledge.

TECHNICAL MEMORANDUMS: Information receiving limited distribution because of preliminary data, security classification, or other reasons.

CONTRACTOR REPORTS: Scientific and technical information generated under a NASA contract or grant and considered an important contribution to existing knowledge.

TECHNICAL TRANSLATIONS: Information published in a foreign language considered to merit NASA distribution in English.

SPECIAL PUBLICATIONS: Information derived from or of value to NASA activities. Publications include conference proceedings, monographs, data compilations, handbooks, sourcebooks, and special bibliographies.

TECHNOLOGY UTILIZATION PUBLICATIONS: Information on technology used by NASA that may be of particular interest in commercial and other non-aerospace applications. Publications include Tech Briefs, Technology Utilization Reports and Notes, and Technology Surveys.

Details on the availability of these publications may be obtained from:

SCIENTIFIC AND TECHNICAL INFORMATION DIVISION

NATIONAL AERONAUTICS AND SPACE ADMINISTRATION

Washington, D.C. 20546